Particle Detection and Measurement: From Low-Energy Nuclear Fusion with STELLA to High-Energy Muon Momentum Calibration with ATLAS

A Thesis Submitted

for Partial Fulfillment of the Requirements

for the

BS-MS Dual Degree Programme

by

Sparsh Gupta
(Roll No. 20201088)

under the supervision of

Dr. Emilien Chapon
(Département de Physique des Particules - DPhP, CEA Paris-Saclay)
&
Dr. Marcel Heine
(Institut pluridisciplinaire Hubert Curien - IPHC, CNRS-Université de Strasbourg)

to

DEPARTMENT OF PHYSICS
Indian Institute of Science Education and Research
Pune - 411 008, INDIA

May 2025

DECLARATION

I hereby declare that the matter embodied in the report entitled “**Particle Detection and Measurement: From Low-Energy Nuclear Fusion with STELLA to High-Energy Muon Momentum Calibration with ATLAS**” are the results of the work carried out by me at the DPhP, CEA Paris Saclay and IPHC, CNRS-UdS, under the supervision of Emilien Chapon and Marcel Heine respectively, and the same has not been submitted elsewhere for any other degree.

Sparsh Gupta

BSMS Student

Roll no. 20201088

IISER Pune. 411008

Dr. Emilien Chapon

Project Supervisor

Researcher, DPhP

CEA Paris-Saclay. 91191

Dr. Marcel Heine

Project Co-Supervisor

Research Scientist, IPHC

CNRS-UdS. 67037

Dr. Seema Sharma

Project Expert

Professor, Dept. of Physics

IISER Pune. 411008

May 2025

Certificate

This is to certify that this dissertation entitled "**Particle Detection and Measurement: From Low-Energy Nuclear Fusion with STELLA to High-Energy Muon Momentum Calibration with ATLAS**" towards the partial fulfillment of the BS-MS dual degree programme at the Indian Institute of Science Education and Research, Pune represents study/work carried out by **Sparsh Gupta** at DPhP, CEA Paris-Saclay and IPHC, CNRS-UdS under the supervision of Emilien Chapon (Researcher, DPhP CEA Paris-Saclay) and Marcel Heine (Research Scientist, IPHC CNRS-UdS) during the academic year 2024-2025.

Sparsh Gupta

BSMS Student

Roll no. 20201088

IISER Pune. 411008

Dr. Emilien Chapon

Project Supervisor

Researcher, DPhP

CEA Paris-Saclay. 91191

Dr. Marcel Heine

Project Co-Supervisor

Research Scientist, IPHC

CNRS-UdS. 67037

ACKNOWLEDGEMENT

This thesis stands as a testament to the collective effort and generosity of those who guided, challenged, and supported me throughout this journey.

My gratitude goes to my supervisors, Dr. Emilien Chapon and Dr. Marcel Heine, whose insights and guidance gave me new learning opportunities. They challenged me to think deeper and their patience during my struggles was instrumental to shape this research. I would also like to thank the STELLA and CEA teams, and the ATLAS Collaboration for providing not just resources, but a vibrant working environment. Special thanks to Dr. Dionysios Fakoudis for his willingness to guide me through codes and concepts whenever I needed. I am thankful to Dr. Seema Sharma for agreeing to be my expert and providing her guidance and feedback throughout the thesis.

To Jhanvee, my partner and voice of reason - your belief in my potential paved way for me to push my limits. Thank you for being my constant motivation, for supporting me through challenges, and for inspiring me to grow both as a researcher and as a person. Our adventures have given me cherished memories and the strength to push forward. I am grateful to my parents as well to provide me with all the resources I needed for pursuing my interest and I could focus without distraction with their support.

Finally, I acknowledge all those whose work contributed to this thesis, directly or indirectly. I am honored to add a small piece to the world of physics research.

Pune - 411 008 **Sparsh Gupta**

May 2025

ABSTRACT

This thesis presents a study of particle detection and measurement spanning from low-energy nuclear fusion experiments at STELLA to high-energy muon calibration studies at the ATLAS detector. The first part of the study focuses on the measurement of the fusion cross-section and spin assignment for the $^{12}C +^{12} C$ reaction at $E_{cm} = 5.02$ MeV using the STELLA experimental setup. Charged particle detection techniques, cross-section evaluation, and Legendre polynomial fits were employed to determine resonance structures in the compound nucleus ^{24}Mg. The results confirm a spin-parity assignment of $J^{\pi} = 2^{+}$, consistent with previous studies, and provide valuable insights for astrophysical models of stellar evolution.

The second part of the study shifts to high-energy physics, focusing on muon momentum calibration at ATLAS for precise Z-boson mass measurements. The calibration technique employs J/ψ decays to address charge-dependent and charge-independent biases in transverse momentum measurements. Using data from Run-2 of the LHC, the analysis refines muon track parameters within the Inner Detector, improving the accuracy of the reconstructed Z-boson mass. This calibration is crucial for reducing systematic uncertainties in electroweak precision measurements, directly impacting the determination of fundamental parameters such as the W-boson mass and weak mixing angle.

Contents

List of Figures

Part I

Measurement of the ^{12}C + ^{12}C Fusion Cross-Section and Spin Assignment at STELLA: Investigation of the Resonant Compound State at E_{cm} = 5.02 MeV

Chapter 1

Introduction

The fusion of carbon-12 (^{12}C) nuclei is a fundamental process in the late stages of stellar evolution in massive stars undergoing carbon burning. Despite its crucial role, accurately determining the reaction rates at low energies remains challenging, particularly in regions where resonances dominate the cross-section. Precise measurements of these reaction rates are essential for improving stellar evolution models and understanding nuclear abundances in stars.

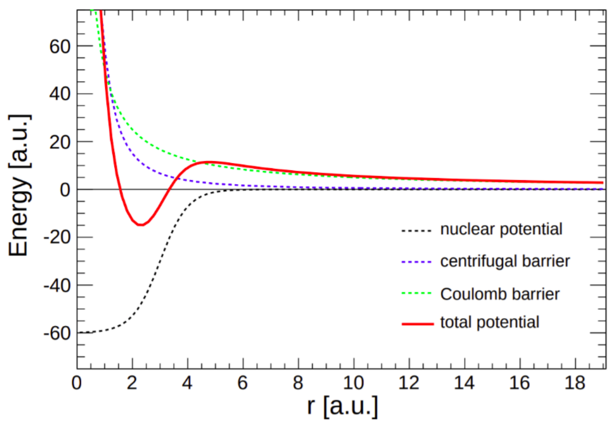

Figure 1.1: Effective nuclear potential for a fusion reaction. [1]

Fig 1.1 illustrates the effective potential that a nucleus faces for fusion to occur. Due to the short-range of the nuclear potential, the nucleus must first overcome the long-range Coulomb barrier (as well as the Centrifugal barrier) to reach the attractive potential well. At low astrophysical energies, which is typical in stars, overcoming this barrier is improbable; hence, the fusion reaction must proceed via quantum tunneling, allowing the nuclei to bypass the repulsive forces. The STELLA experiment (2), therefore, focuses on measuring the cross-section of ^{12}C fusion at low energies (E_{CM} = 3.5 to 20 MeV). Carbon burning in stars may occur through four channels [1], [2]:

$$^{12}_{6}C +^{12}_{6} C \rightarrow^{24}_{12} Mg^{*} \rightarrow^{20}_{10} Ne + \alpha + \gamma \ (Q_{\alpha} =) + 4657.47\, keV \tag{1.1}$$

$$^{12}_{6}C +^{12}_{6} C \rightarrow^{24}_{12} Mg^{*} \rightarrow^{23}_{11} Na + p + \gamma \ (Q_{p} =) + 2207.641\, keV \tag{1.2}$$

$$^{12}_{6}C +^{12}_{6} C \rightarrow^{24}_{12} Mg^{*} \rightarrow^{23}_{12} Mg + n + \gamma \ (Q_{n} =) - 2570.923\, keV \tag{1.3}$$

$$^{12}_{6}C +^{12}_{6} C \rightarrow^{24}_{12} Mg + \gamma \ (Q_{\gamma} =) + 13972.41\, keV \tag{1.4}$$

$$^{12}_{6}C +^{12}_{6} C \rightarrow^{24}_{12} Mg^{*} \rightarrow^{16}_{8} O + 2^{4}_{2}He \ (Q_{O} =) - 0.113\, MeV \tag{1.5}$$

The neutron channel (Eq.1.3) has a very small cross-section at low energies due to its endothermic nature, while the gamma channel (Eq.1.4) is improbable as it proceeds via electromagnetic interaction [3]. The alpha and proton channels (Eq.1.1, Eq.1.2) dominate the fusion reactions, proceeding via the formation of a compound nucleus, $^{24}_{12}$Mg, which subsequently decays into lighter nuclei. Reactions 1.1 & 1.2 will be the focus of our measurements. In these reactions, there are multiple exit channels such as the α_0, α_1, α_2, ... and p_0, p_1, p_2, and so on. The α_0 reaction refers to the emission of an alpha particle leaving the residual $^{20}_{10}$Ne nucleus in its ground state, while the α_1 reaction involves alpha emission with the residual $^{20}_{10}$Ne nucleus in its first excited state. This is followed by the emission of a γ-particle with corresponding energy due to the de-excitation of the daughter nuclei. Similarly the other channels are defined (Fig 1.2).

The final reaction (Eq.1.5) is also improbable because it is endothermic as well as involves three reaction products. If we consider the reaction occurring in reverse, it would require all three products to converge simultaneously, which is less likely than two-body interactions.

1.1 Theoretical Framework

Understanding the branching of these reaction channels is necessary for determining the energy distribution of the products and for constraining the spin-parity assignments of the resonant

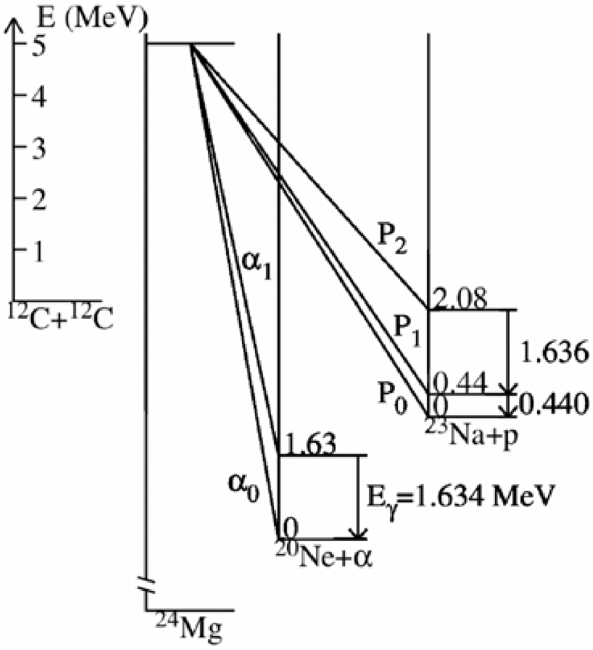

Figure 1.2: Energy Level diagram of the decay of $^{24}_{12}$Mg excited after a $^{12}_{6}$C + $^{12}_{6}$C fusion reaction. [4]

states in the compound nucleus $^{24}_{12}$Mg. The corresponding particle energy (E_3) in the laboratory frame, for a non-relativistic nuclear reaction, 1+2 $\rightarrow$ 3+4, can be predicted from the experiments through kinematic calculations (Eq.1.6):

$$E_3(\theta_3) = \frac{A_1 A_3 E_{cm}}{A_2(A_1 + A_2)} \frac{\left(\gamma_3 \cos(\theta_3) \pm \sqrt{1 - \gamma_3^2 \sin^2(\theta_3)}\right)^2}{\gamma_3^2} \tag{1.6}$$

Here, E_{cm} is the center of mass energy, A_1 and A_2 are the mass numbers of the incident nuclei, A_3 & θ_3 is the mass number and laboratory angle of the detected particle (α or p) and $\gamma_3 = \sqrt{\frac{A_1 A_3}{A_2 A_4} \frac{E_{cm}}{E_{cm}+Q}}$ is the kinematic factor, with A_4 the mass number of the daughter nuclei. Q is the Q-value of the reaction, taking in to account the excitation level of the daughter nuclei.

1.1.1 Fusion Cross Section

To fully describe the reaction probability, we must consider the fusion reaction cross-section. The differential cross-section is determined experimentally using (Eq.1.7):

$$\left(\frac{d\sigma}{d\Omega}\right)_{lab} = \frac{S}{I \times N_t \times \Delta\Omega} \tag{1.7}$$

Where S is the number of counts in the exit channel measured, I is the number of beam particles measured from the integrated intensity, N_t is the number of nuclei in the target per surface and $\Delta\Omega$ is the solid angle covered by the detector.

These cross-sections are measured in the laboratory frame and must be transformed in the center of mass frame for analysis using Eq.1.8. Similarly, in the laboratory frame, the angle of the detected particle, θ_{lab}, is defined relative to the beam axis, with the collision point at the origin of the coordinate system and can be transformed using Eq.1.9.

$$\left(\frac{d\sigma}{d\Omega}\right)_{cm} = \left(\frac{d\sigma}{d\Omega}\right)_{lab} \frac{\sqrt{1-\gamma_3^2 \sin^2\theta_{lab}}}{\left(\gamma_3 \cos\theta_{lab} \pm \sqrt{1-\gamma_3^2 \sin^2\theta_{lab}}\right)^2} \tag{1.8}$$

$$\theta_{cm} = \sin^{-1}\left[\sin\theta_{lab}\left(\gamma_3 \cos\theta_{lab} \pm \sqrt{1-\gamma_3^2 \sin^2\theta_{lab}}\right)\right] \tag{1.9}$$

1.1.2 Total Exclusive Cross-Section and Spin Assignment

In this study, R-Matrix theory is used to analyze the nuclear reaction for modeling the angular distributions of the differential cross-section. R-matrix theory is used in nuclear reaction theory, particularly for analyzing scattering processes and resonance structures. The resonance at E_{cm} = 5.02 MeV can be analytically understood using the Single-Channel R-Matrix Theory [5], used for understanding scattering of spinless particles which is the case for this exit channel, as supported by [6]. The α_0 exit channel represents the simplest solution, as the spin of ${}^{20}_{10}$Ne is zero. The differential cross-section (Eq.1.10) is governed by the collision matrix U_ℓ, where ℓ represents the orbital angular momentum quantum number of each *external* partial wave (ℓ = even, since the incoming bosons are identical, the wave function has to be symmetric). In this formalism, space is divided into two regions: the *internal region*, where nuclear interactions occur, within a radius R_a, and is typically modeled by compound nucleus states and a square well potential; and the external region, where particles scatter freely, described by scattering states. The external wave function is described as a superposition of incoming and outgoing spherical waves that lie *outside* the nuclear interaction region. The collision matrix encodes the effects of the interaction on these waves, linking the asymptotic behavior of the wave function outside the nuclear interaction region with the *internal* potential, where the compound nucleus occurs.

$$\frac{d\sigma}{d\Omega} = \left(\frac{1}{4k^2}\right) \left| \sum_{\ell=even} (2\ell+1)(1-U_\ell)P_\ell(\cos\theta) \right|^2 \tag{1.10}$$

The total exclusive cross section can be calculated by integration:

$$\sigma = \int \left(\frac{d\sigma}{d\Omega}\right) d\Omega = \left(\frac{\pi}{k^2}\right) \sum_{\ell=even} (2\ell+1) \left|1-U_\ell\right|^2 \tag{1.11}$$

k represents the wave number of the plane wave and P_ℓ are the Legendre polynomials. Coefficients of P_ℓ indicate the contribution of each partial wave to the measured cross-section at the respective resonance. In this study, we analyze these coefficients to determine which orbital angular momenta states of the compound nucleus are responsible for the resonance, also known as Spin assignment.

For the remaining exit channels we use a more general formalism of nuclear reactions, the Multi-Channel R-Matrix Theory [5]. Unlike the Single-Channel R-Matrix theory that only considers one reaction or scattering process, Multi-Channel R-matrix theory accounts for multiple reactions or scattering processes, allowing the interaction between different channels to be modeled simultaneously. The differential cross-section and the total exclusive cross-section can be respectively calculated by:

$$\frac{d\sigma}{d\Omega} = \sum_{\ell=even}^{\ell_{max}} B_\ell P_\ell(\cos\theta) \tag{1.12}$$

$$\sigma = 4\pi B_0 \tag{1.13}$$

The coefficients, B_ℓ, depend on the spin and the nuclear states of the reactants and products. In our case, the spin assignment is not definite and the angular momentum is constrained only by a lower limit (Eq.1.14). This is based on the calculations shown in [7].

$$\ell_{max} \leq \min(2J \equiv 2\ell_i, 2\ell_o) \tag{1.14}$$

J represents the angular momentum of the compound state which is equivalent to the orbital angular momentum of the incident nuclei, ℓ_i, and ℓ_o is the orbital angular momentum of the outgoing nuclei. The resonance at E_{cm} = 5.02 MeV in our study can then be explained using the corresponding resonant state deduced after the spin assignment which will be done after the differential cross-section is fit using Legendre polynomials.

Chapter 2

Experimental Setup - STELLA

The STELLA (STELlar LAboratory) collaboration based in Andromede Facility at IJCLab Orsay, France, studies nuclear reactions at Sub-Coulomb energies (3.5 – 20 MeV), measuring cross-section up to the order of milibarns! It uses coincidence measurement techniques to detect evaporated charged particles and the gamma from de-excitation of the daughter nuclei. For charged particle detection, thin target foils (30 – 50 $\mu g/cm^2$) are used to minimize energy loss in the target. The measurement statistics drop exponentially with energy and are very sensitive to impurities & background contamination. The reaction chamber is evacuated so that the α-particles and protons are not disturbed (Fig 2.1).

The target is placed at the center of the reaction chamber and is rotated via magnetic motor couple to it outside the chamber. This is done to prevent degradation of the target. The reaction chamber is covered by a 1.5 mm thick aluminum dome to minimize the absorption of gamma rays that are detected by $LaBr_3$ (Ce) scintillator detectors outside the dome. [1]

2.1 Charged Particle Detection

Charged particles are detected using three Silicon Strip detectors in the reaction chamber (Fig 2.3); two of them are Double Sided Striped Silicon Detectors (DSSSD) S3 types (Fig 2.2) and one DSSSD S1. The S3 detectors are positioned at forward (S3F) and backward (S3B) directions with respect to the beam while the S1 detector is placed between the target and the S3B detector.

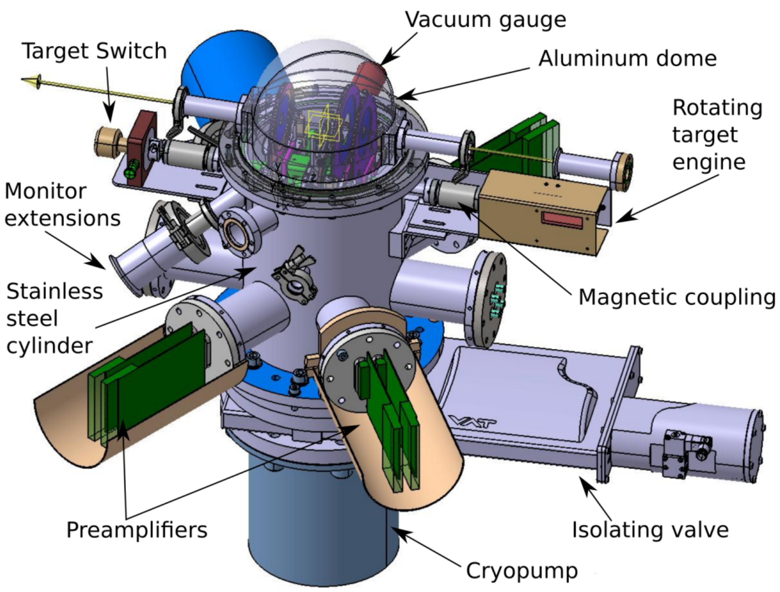

Figure 2.1: 3D CAD Representation of the reaction chamber. [1]

Strip detectors measure the position and energy of charged particles by collecting the ionization of electron-hole pairs they cause in the detector material and the resulting signal collection in the strips. The S3F and S3B detectors have 24 complete rings, each having a width of 986 μm with a 100 μm resistive separation, covering the angles $\theta_{lab} = 10.4^o - 30.3^o$ and $\theta_{lab} = 148^o - 169^o$ respectively. The S1 detector has 16 complete rings each having a width of 1505 μm with a 96 μm resistive separation, covering the intermediate angles $\theta_{lab} = 122.4^o - 141.8^o$. Both the S3B and S1 detectors are covered with a 0.8 μm thick aluminum foil, which blocks electrons emitted when the beam strikes the target. This thickness is optimized to prevent significant energy loss due to straggling in the foil. In the S3F detector, which is positioned in the forward direction, the particles are more energetic and hence requires additional protection. It must stop not only electrons but also elastically scattered ^{12}C nuclei. Therefore, a thicker 10 μm aluminum foil is used to effectively shield the detector without compromising the accuracy. Only the data from S3F and S3B detectors were available during this study.

2.2 Gamma Ray detection

Surrounding the aluminum dome is the UK-FATIMA (FAst TIMing Array) detectors, a hemispherical array of 36 $LaBr_3$(Ce) scintillator detectors that measure gamma rays from the de-excitation of the daughter nuclei. Detection is done by converting the energy of the gamma

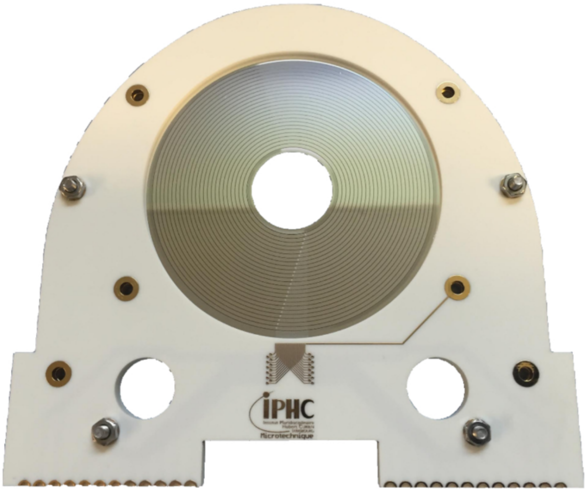

Figure 2.2: Photograph of the S3 detector on the junction side, the rings visible are the strip detectors. [1]

photons into visible light through scintillation, and then converting that light into an electrical signal using a photomultiplier tube. Fast timing is essential in this experiment to accurately associate gamma rays with specific fusion events, discriminate against background or uncorrelated signals, and allow coincidence analysis with the silicon detectors. The fast timing of $LaBr_3$(Ce) allows us to achieve precision and sensitivity required for measuring fusion reactions. Although, the current analysis does not use the data from UK-FATIMA and only charged particle data is used for the cross-section measurement.

2.3 Beam Intensity

Methane gas is ionized using an Electron Cyclotron Resonance (ECR) source, and the resulting ions are accelerated and filtered using a 4 MeV electrostatic Pelletron© accelerator to create a pure carbon beam. Two Faraday cups, positioned upstream and downstream of the reaction chamber (Fig 2.4), measure the electric current, which corresponds to the charged state and the number of beam particles passing through.

The number of incident beam particles is given by Eq.2.1, where $Q_{CI} = 10^{-10}\,C$ is the current conversion ratio, q_2 ($\approx 4.4^+$, in this study) is the average charge state of the beam after passing through the target, e the electric charge and N_{CI} is the number of counts given by integrator at the end of measurement.

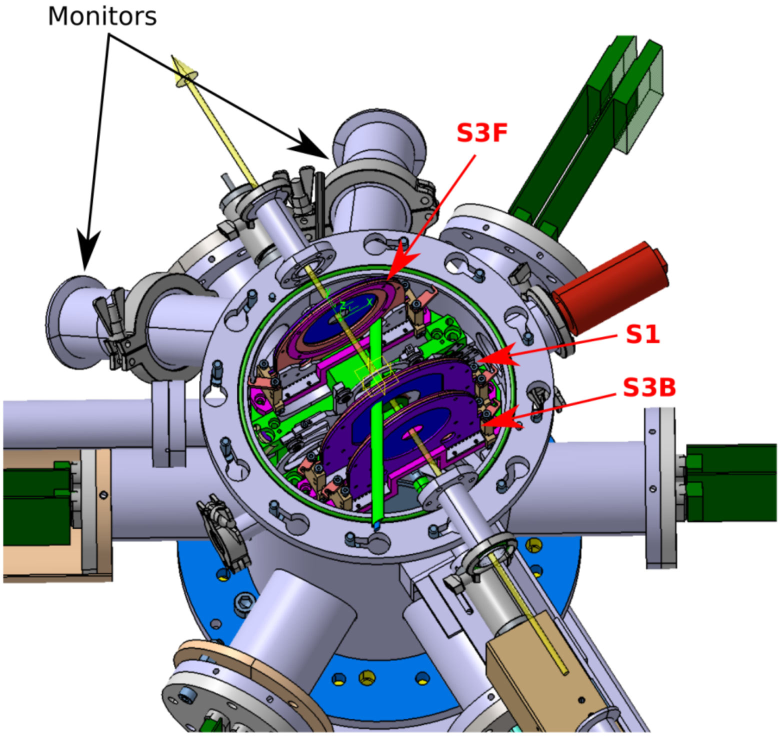

Figure 2.3: 3D CAD Representation of the reaction chamber inside the dome, highlighting the Strip detectors in red for charged particle detection. [1]

$$I = N_{beam} = \frac{N_{CI}}{Q_{CI} \times e \times q_2} \sim 1.818 \times 10^{15} \tag{2.1}$$

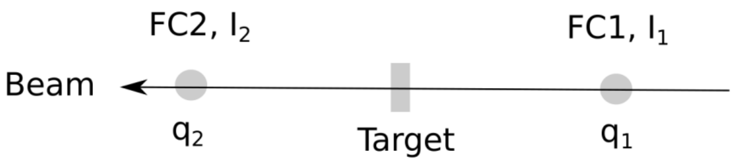

Figure 2.4: Farday Cup integrator Scheme at STELLA. [1]

Chapter 3

Data Analysis

Previous measurements by Becker et al. [8] & Mazarakis et al. [9], conducted at E_{cm} = 5 MeV and E_{cm} = 4.91 + 0.075 MeV (Correction from [10]) respectively, were considered as comparison to the data collected in Run 10 of the STELLA Experiment. Fig 3.1 illustrates the energy distribution of the total exclusive cross-section for the α_0 channel as shown in [8] and a resonance peak is observed at E_{cm} = 5 MeV, motivating the investigation of the resonance structure of the compound nucleus $^{24}_{12}$Mg.

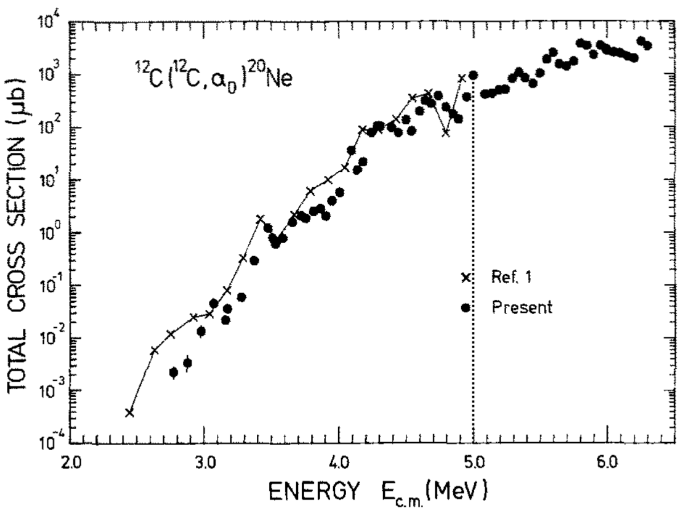

Figure 3.1: Angle-integrated excitation function for the α_0 channel as measured in Becker et al. [8]

The angular distribution of the differential cross-section for the α_0 exit channel at E_{cm} = 5 MeV from past experiments were digitized, reproduced and fit using Eq.1.12 to give:

- **Becker et al.** [8] - Total reported cross-section, σ_{α_0} = 0.95 mb

  Total cross-section calculated after digitization, σ_{α_0} = 0.949±12.66% mb (using ℓ_{max} = 4)

  These values were obtained after obtaining the best value of ℓ_{max}, which was decided after no significant improvement in χ^2 was seen.

ℓ_{max}	χ^2, **Becker et al.**	χ^2, **Digitization**
0	0.308	1.977
2	0.127	0.633
4	0.0007	0.0018
6	0.0007	0.0011
8	0.0004	0.0011

- **Mazarakis et al.** [9] - Total reported cross-section, σ_{α_0} = 0.840 mb

  Total cross-section calculated after digitization, σ_{α_0} = 0.766 ± 8.59% mb (using ℓ_{max} = 4)

ℓ_{max}	χ^2, **Digitization**
0	0.534
2	0.064
4	0.011
6	0.0094
8	0.0087

  The cross-section from Mazarakis et al.[9] is measured different because the fitting scheme and the Center of Mass energy used by the author was different and might be outdated, there may also be variations due to digitization.

3.1 Energy Spectrum

Fig 3.3 shows the typical spectra for one of the S3F detectors. Each peak corresponds to one of the charged particles from the decay of the compound nucleus, $^{24}_{12}$Mg. These particles can be identified using the energy prediction we obtain from Eq.1.6.

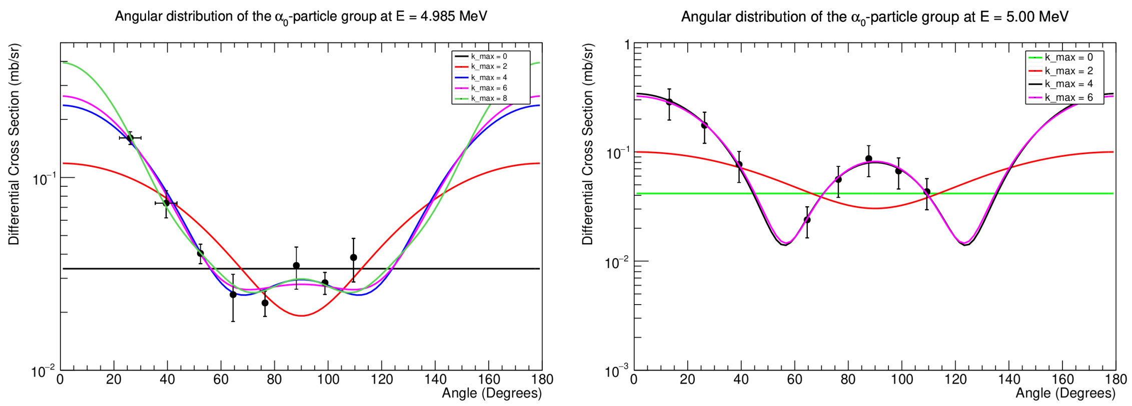

(a) Mazarakis et al. [9]

(b) Becker et al. [8]

Figure 3.2: Angular Distribution of the differential cross-section after digitization along with the Legendre Polynomial fits.

3.1.1 Coincidence Analysis

This analysis aims to improve the identification of correlated gamma rays and charged particles by enhancing the timing resolution of the detector system, which is essential for selecting fusion events. Coincidence events are selected within a 400 ns time window—typical for physical correlations. Two complementary methods are used to correct timing mis-alignments across detector strips. The first method exploits charge-sharing events between neighboring strips in the silicon detector: when a single particle deposits charge across two strips, known as multiplicity two events, the time difference between their signals can be used to align the strip timings. Repeating this across all strips achieves a precise timing calibration with a resolution of 10^{-15} ns. The second method directly compares the time difference between gamma rays and charged particles for known exit channels, using narrow energy selections and fitting the timing peak with a Gaussian function to extract corrections for each strip. These corrections significantly reduce the contribution of random, non-correlated background events and allow for more accurate identification of channels like α_1 and p_1, which may overlap in energy but differ in timing.

One might observe that the peaks of multiplicity two and multiplicity three events in the histogram are not aligned with the peaks of multiplicity one events. The shift arises because the signals are normalized and offset using a linear function ($f(x) = ax + b$) to convert them into counts. However, due to charge sharing among neighboring detectors, the offset is effectively counted multiple times. For multiplicity two events, we expect $f(x_1 + x_2) = a(x_1 + x_2) + b$ but

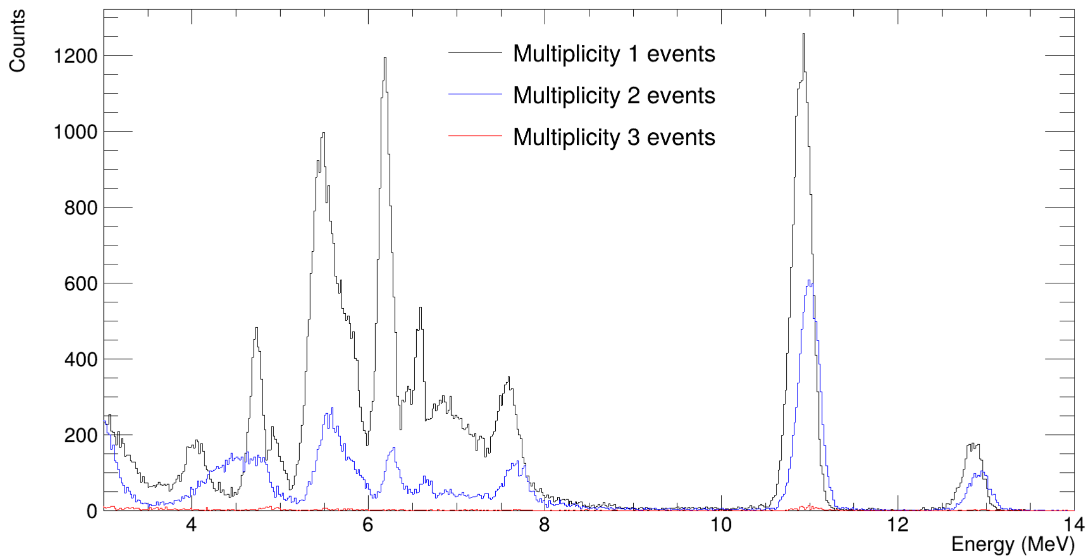

Figure 3.3: Typical Energy Spectrum of one of the strip detectors with Multiplicity one, two and three events.

since the detector is triggered twice the actual outcome is $f(x_1)+f(x_2) = a(x_1)+b+a(x_2)+b = a(x_1 + x_2) + 2b$, the extra offset needs to be removed. This was corrected by shifting the multiplicity two and multiplicity three events by a constant factor after fitting them with a Gaussian Function and a Linear Background.

3.2 Cross-Section Evaluation

Histograms were obtained for the channels α_0, p_0, and p_1, which were subsequently fit using a Gaussian function on a defined energy selection, along with a linear background. The Gaussian fits were integrated to determine the number of counts in each exit channel at a given angle.

To calculate the cross-section using Eq.1.7, the solid angles were derived from simple geometry of the experimental setup. The beam intensity was measured using the Faraday cup integrator to be $I \approx 1.818 \times 10^{15}$and the target number density was $N_t \approx 1.504 \times 10^{18}$ cm^{-2}. Finally, after applying the kinematic boosts using Eq.1.8 & Eq.1.9, the differential cross-section distributions were obtained in the center of mass frame (Fig 3.5).

The detector effects and corrections that were considered are listed below:

- The guard rings, that separate the detector edges, in the detectors, although part of the

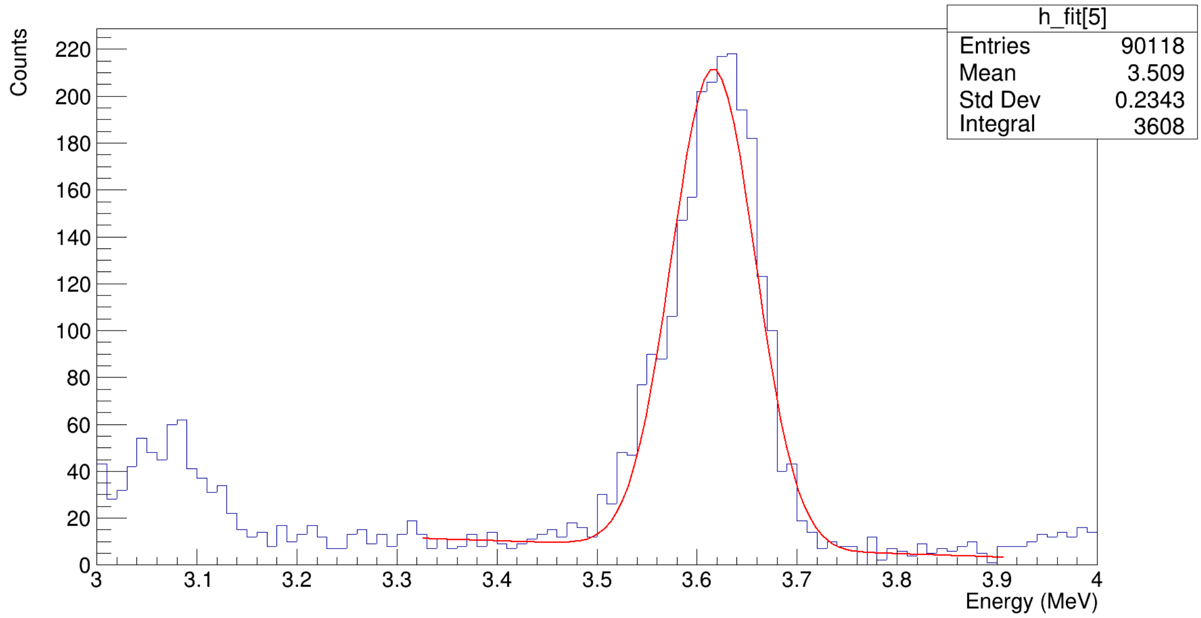

Figure 3.4: Fits for one of the detector peaks for the α_0-channel.

active region, were not biased; consequently, the counts from both the innermost and outermost rings were low. Hence, these data points were excluded from the Legendre polynomial fits.

- It was identified that one of the detector strips had a shrunken depletion region (due to charge build-up); therefore, this detector was excluded from the analysis.

- The active region of the S3 detectors were not well defined in the documentation. To address this issue, a sensitivity test was performed, which indicated that this correction had minimal impact on the distribution.

- Sensitivity tests of the beam energy were also conducted; however, no significant effects were observed.

- Due to the high momentum of the protons, they are able to punch through the detector without being detected at forward angles. As a result, no distinguishable peak was observed in the energy spectrum, or there were low counts for the p_0 and p_1-channels at smaller forward angles ($\theta < 30^o$). Consequently, these low-count data points were excluded from the analysis.

3.2.1 Legendre Polynomial Fits

After calculating the differential cross-section for the three exit channels, the fit routine was conducted for Spin assignment and obtaining the total exclusive cross-sections. As described in 1.1.2, α_0 exit channel is modeled using the Single-Channel R-Matrix Theory, Eq.1.10 & Eq.1.11, whereas the p_0 and p_1 channels by the Multi-Channel R-Matrix Theory, Eq.1.12 & Eq.1.13. Using χ^2-analysis (Eq.3.1), the values of ℓ (the orbital angular momentum number) were constrained until no further improvement in the fit was seen. The same constraints were then applied to calculate the total exclusive cross-section. The resulting fits with the different selection of ℓ_{max} can be seen in Fig 3.5.

$$\chi^2 = \sum_i \frac{(O_i - E_i)^2}{E_i}, \quad O_i = \text{Observed Values} \ \& \ E_i = \text{Expected Values} \tag{3.1}$$

The final value of ℓ_{max} was determined based on the minima of the χ^2 value (Table 3.2.1), as done in [8]. It is worth noting that after the initial few fits, the χ^2 value essentially plateaus and remains constant. Therefore, only the value that showed a significant decrease compared to the previous Legendre fit was chosen. Despite the low χ^2 values, some nonphysical fits were excluded. For example, for the p_1-channel with $\ell_{max} = 4$, the cross-section became negative, which is non-physical.

ℓ_{max}	χ^2, α_0-channel	χ^2, p_0-channel	χ^2, p_1-channel
0	0.01160	0.006950	0.00701
2	0.00264	0.000329	0.00281
4	0.00254	0.000328	0.00177
6	0.00220	0.000332	0.00178
8	0.00216	0.000294	0.00135

Table 3.2.1. χ^2 values for all the Legendre fits performed on the Differential Cross-section data obtained after the analysis.

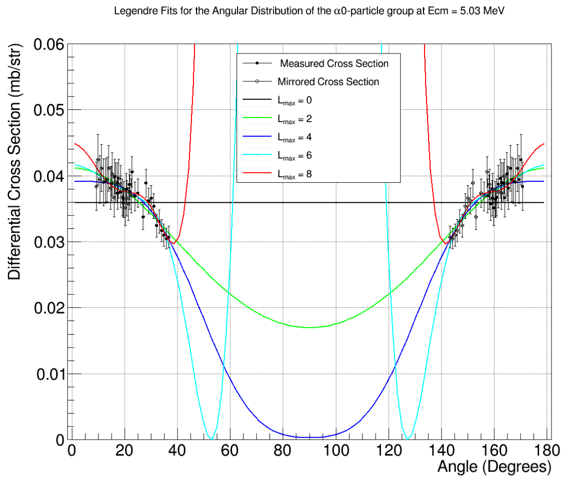

(a) α_0-channel

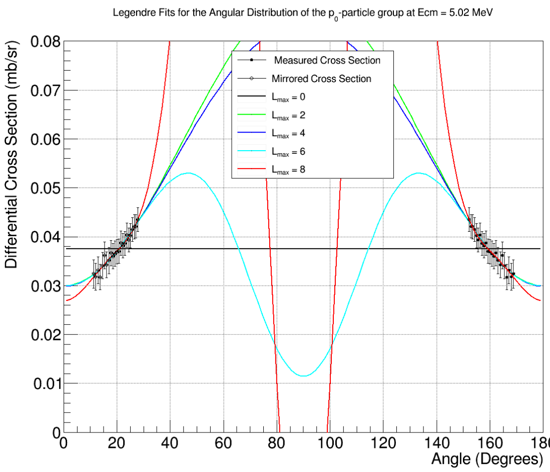

(b) p_0-channel

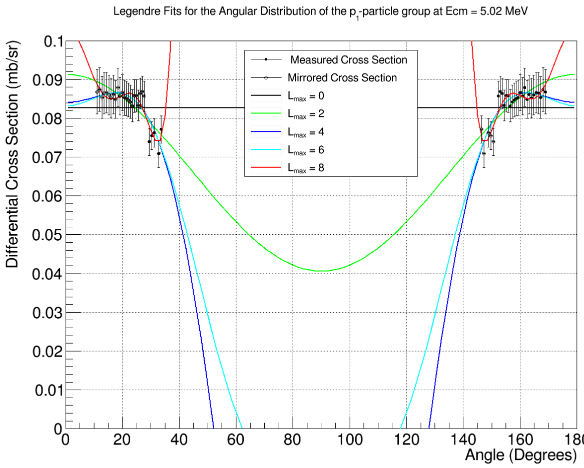

(c) p_1-channel

Figure 3.5: Legendre polynomial fits (Eq.1.10 and 1.12) for the Angular Distribution of the cross-section.

Chapter 4

Results and Discussion

4.1 Total Exclusive Cross-Section

The total cross-section was evaluated using Eq.1.11 for the α_0-channel and using Eq.1.13 for the p_0 & p_1-channels. The value of ℓ_{max} in each case was determined using the optimal Legendre fit (Fig 4.1) based on the χ^2-analysis done in 3.2.1. The total exclusive cross-sections obtained are:

- $\ell_{max} = 2$, $\boldsymbol{p_1}$**-channel:** $\sigma_{p_1} = 0.7230 \pm 9.14\%$ mb
- $\boldsymbol{\alpha_0}$**-channel:** $\sigma_{\alpha_0} = 0.3059 \pm 6.51\%$ mb
- $\ell_{max} = 2$, $\boldsymbol{p_1}$**-channel:** $\sigma_{p_1} = 0.7230 \pm 9.14\%$ mb
- $\boldsymbol{p_0}$**-channel:** $\sigma_{p_0} = 0.8772 \pm 7.62\%$ mb
- $\ell_{max} = 2$, $\boldsymbol{p_1}$**-channel:** $\sigma_{p_1} = 0.7230 \pm 9.14\%$ mb
- $\boldsymbol{p_1}$**-channel:** $\sigma_{p_1} = 0.7230 \pm 9.14\%$ mb

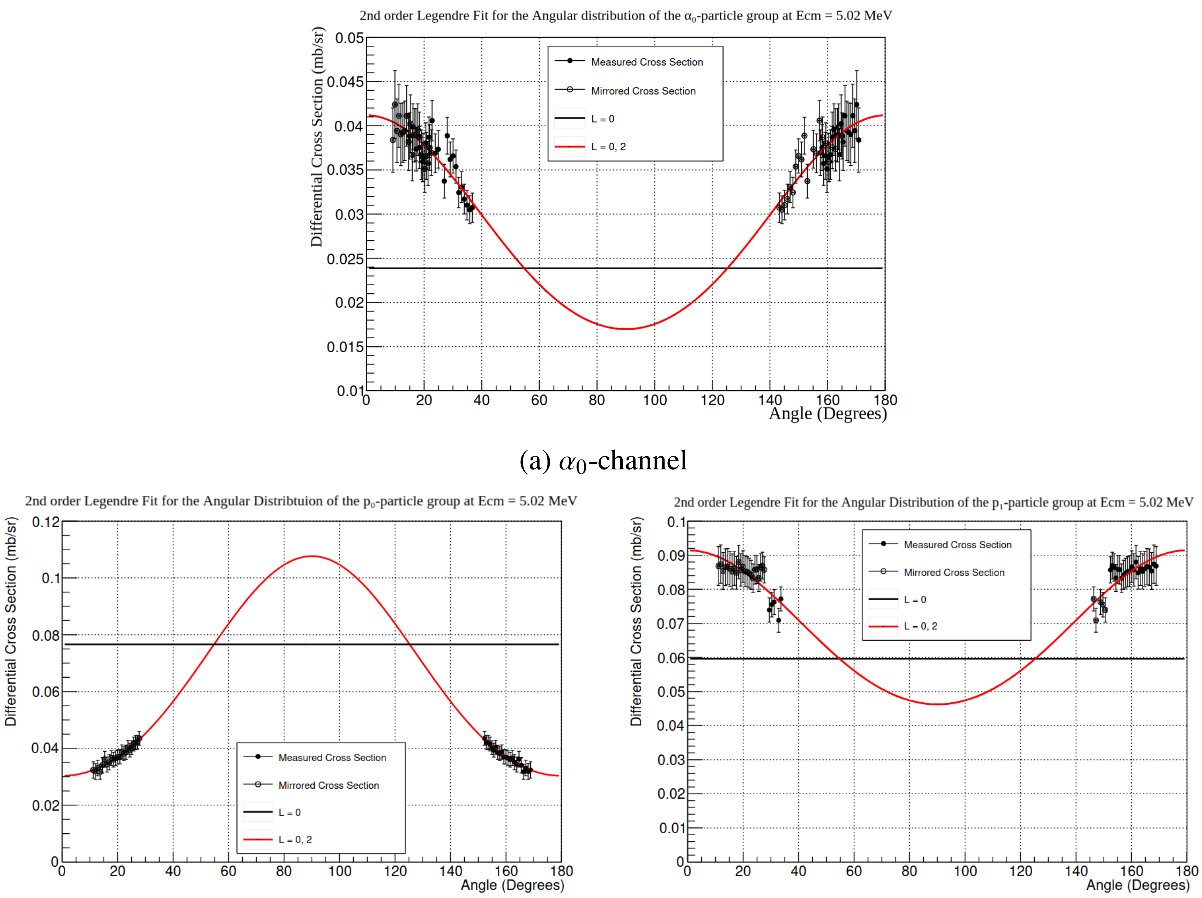

(a) α_0-channel

(b) p_0-channel

(c) p_1-channel

Figure 4.1: 2nd Order Legendre polynomial fits for the Angular Distribution of the cross-section.

4.1.1 Background Estimation

The cross-sections obtained are influenced by background, especially in the proton channels. A significant source of this background comes from water contamination in the target. The protons produced in the reaction $^{12}C + d \rightarrow^{13} C + p$ have energies very similar to those in the proton channel. Additionally, several resonance peaks overlap at lower energies making it difficult to resolve the desired peaks (Fig. 3.3).

The S3B detector was also noisy, mainly because less events were observed at backward angles due to the high forward scattering angles of the reactions. However, background noise was significantly reduced through energy selection and by fitting a linear background model. Gamma particles emitted from the excited states of $^{20}_{10}$Ne may not be detected, leading to the mis-identification of $\alpha_1, \alpha_2, \ldots$ particles as α_0 particles. Coincidence selection was used to reduce such mis-identifications and improve accuracy of reaction kinematics.

4.2 Spin Assignments

- **α_0-channel:** Based on the value, $\ell_{max} = 2$, we can deduce the spin-parity of the compound nucleus, $^{24}_{12}$Mg, to be, $J^\pi = 0^+$ or 2^+ from the corresponding contribution of the partial waves. Parity will always remain positive since the incoming nuclei, $^{12}_{6}$C, are identical and the intrinsic parity is also +1.
- **p_0-channel:** With $\ell_{max} = 2$ and using the constraint given in Eq. 1.14, we find that $J \geq 1$. Therefore, the possible values of J^π are $2^+, 4^+, 6^+, \ldots$
- **p_1-channel:** With $\ell_{max} = 2$, and using the same logic as for the p_0-channel, the possible values of J^π are $2^+, 4^+, 6^+, \ldots$

The final Spin Assignment for the compound nucleus, $^{24}_{12}$Mg, formed at $E_{cm} = 5.02$MeV after the fusion reaction of ^{12}C +^{12}C is $J^\pi = 2^+$, which is consistent with the results obtained by Becker Et Al. [8], Galster Et Al. [6] and Almqvist et Al. [11].

4.3 Discussion

The accuracy and precision of cross-section measurements allow for more reliable determination of the S-factor (or Astrophysical factor), which in turn aids in evaluating the consistency and accuracy of studies related to fusion suppression (or hindrance effect) [12] and resonances in stellar evolution. The S-factor is used to isolate nuclear effects on the cross-section by compensating for the energy dependence caused by the exponential decrease in the cross-section due to tunneling through the Coulomb barrier. It is expressed by the following equation:

$$\sigma(E) = \frac{S(E)}{E} \exp\left(-2\pi\eta\right) \tag{4.1}$$

where $S(E)$ is the S-factor, $\sigma(E)$ is the cross-section, E is the energy of the reaction, η is the Sommerfeld parameter.

Pignatari et al. [13] conducted a study using the GENEC code [14] to show that changes in the alpha-to-proton ratio can significantly affect stellar evolution and nucleosynthesis. Such shifts can produce neutrons in the stellar environment, which then trigger important secondary reactions, especially when the alpha channel is more dominant. This study demonstrates that the alpha/proton ratio can evolve considerably over time and are sensitive to the reaction rates of fusion reactions. Through the given spin assignments and cross-sections, one can interpret energy levels, resonances, and reaction rates, which are essential for understanding nuclear structure, reaction mechanisms, and nuclear abundances in stars.

Part II

Muon Momentum Calibration at ATLAS for Z-mass Measurement

Chapter 5

Introduction

The measurement of the Z-boson mass is very important in the Standard Model of particle physics, providing a critical test of electroweak theory and serving as a probe for numerous theoretical and experimental calculations. Achieving higher accuracy in this measurement directly impacts constraints on fundamental parameters, including the W-boson mass, weak mixing angle, lepton universality and Higgs boson mass predictions.

At the Large Hadron Collider (LHC), Z bosons are produced primarily through quark anti-quark annihilation ($q\bar{q} \rightarrow Z$), but also through higher-order processes such as gluon-gluon fusion ($gg \rightarrow Z$) and associated production with other particles ($pp \rightarrow Z + X$). Once produced, the Z boson decays almost instantly, with a significant fraction undergoing hadronic decays, although the leptonic decays ($Z \rightarrow e^+e^-,\ Z \rightarrow \mu^+\mu^-$) provide clean experimental signatures and are primarily used for precision measurements. In the ATLAS experiment, precise measurements of Z boson properties allow for tests of electroweak interactions in the Standard Model and provide inputs for calibrating detector performance. These calibrations are crucial for reducing systematic uncertainties, ultimately improving the precision of fundamental measurements.

This thesis aims to improve the accuracy of the Z boson mass measurement by refining the calibration of muon momentum. The focus is on reducing uncertainties in the transverse momentum of muons (p_T^μ) through a dedicated calibration procedure. This procedure specifically addresses charge-independent effects and the J/ψ resonance in the muon spectrum, detected by the Inner Detector (ID), is used as a reference for the calibration.

5.1 Theoretical Framework

5.1.1 Standard Model

The Standard Model of particle physics is a successful theoretical framework that describes the fundamental particles and their interactions (Fig 5.1), excluding gravity. The model includes two types of particles: fermions, which make up matter, and bosons, which mediate the interactions. Fermions are divided into quarks, which carry both electric and color charges and form hadrons like protons and neutrons, and leptons, which interact via the electroweak force. The fermions are organized into three generations, each comprising one charged lepton, one neutrino, and two quarks.

In addition to fermions, the SM predicts the existence of elementary bosons. The photon mediates the electromagnetic force, gluons mediate the strong force between quarks, and the weak force is mediated by the W± and Z bosons, predicted by the Glashow-Weinberg-Salam (GWS) theory. A key feature of the SM is the Higgs boson, which is responsible for giving mass to the W± and Z bosons through the Brout-Englert-Higgs mechanism (spontaneous symmetry breaking). The W± and Z bosons were discovered at CERN in 1983, and the Higgs boson, the final missing piece, was discovered in 2012 at CERN, confirming the Standard Model's predictions.

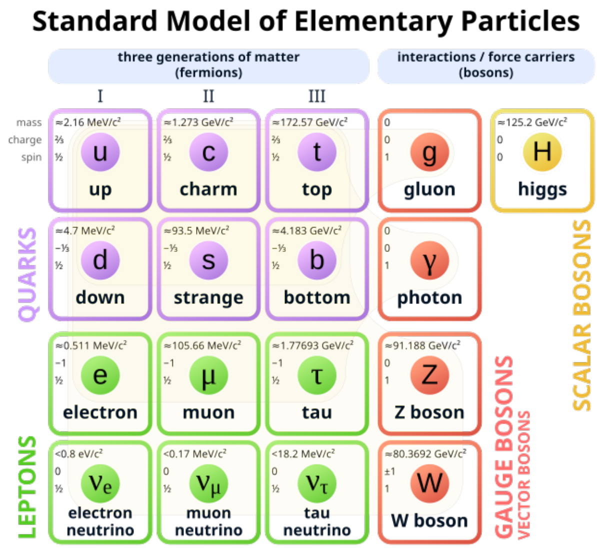

Figure 5.1: Elementary Particles predicted by the Standard model. [15]

5.1.2 Electroweak Sector

The Electroweak (EW) theory unifies two of the four fundamental forces, electromagnetism and the weak nuclear force, into a single framework, as proposed by Glashow, Salam, and Weinberg in the 1960s. It is based on the $SU(2) \otimes U(1)$ gauge group, with weak isospin (T) and weak hypercharge (Y) as generators. These lead to the massless gauge bosons: W_1, W_2, W_3, and B, which are then transformed through spontaneous symmetry breaking into the physical bosons: W^+, W^-, Z^0, and γ. The weak hypercharge (Y) is related to the electric charge (Q) and weak isospin (I_3) by $Y = 2Q - I_3 Y$, and the physical bosons are defined as linar combinations of the gauge fields:

$$A_\mu = B_\mu \cos\theta_W + W_\mu^3 \sin\theta_W \quad \text{(photon, } \gamma\text{)} \tag{5.1}$$

$$Z_\mu = W_\mu^3 \cos\theta_W - B_\mu \sin\theta_W \quad \text{(Z-boson).} \tag{5.2}$$

The weak interactions involve probability currents, where the coupling between the Z-boson and fermions is expressed as:

$$J_\mu^Z = g_Z \left(c_L \bar{\psi}_L \gamma_\mu \psi_L - c_R \bar{\psi}_R \gamma_\mu \psi_R \right), \tag{5.3}$$

showing asymmetry between left- and right-handed fermions. The Electroweak Lagrangian, ignoring mass terms, is written as:

$$\mathcal{L}_{EW} = -\frac{1}{4} W_{\mu\nu}^a W^{a\mu\nu} - \frac{1}{4} B_{\mu\nu} B^{\mu\nu} + i\bar{\Psi}\gamma^\mu D_\mu \Psi. \tag{5.4}$$

The Higgs mechanism is introduced to give mass to the gauge bosons and fermions, solving the mass problem through spontaneous symmetry breaking. The process involves adding a scalar field, and through the interaction with the Higgs field, particles acquire mass. The SM observables are hence correlated with higher order loop diagrams further convoluting these correlations.

5.2 W and Z-Bosons

To validate the Standard Model, its parameters must be measured both independently and together. An example in context of this thesis is the W mass, which is analyzed in parallel with the Z mass (m_Z) in ATLAS, particularly during calibration. The W mass (m_W) is related to parameters such as m_Z, fine-structure constant α_{em}, and the Fermi constant (G_F), with corrections for radiative effects encapsulated in the Δr parameter. These corrections arise from loop diagrams, especially contributions from loop diagrams, specifically contributions from the top quark and the Higgs boson. The relation between m_W, m_Z, and Δr is given by:

$$m_W^2 = C\left(1 - \frac{m_W^2}{m_Z^2}\right)(1 - \Delta r) \tag{5.5}$$

This implies that the precision in the measurement of m_W is also dependent on the uncertainties of m_Z. Currently, at ATLAS, the measurement of m_W (Fig 5.2) is more precise than that from LEP [16], thanks to the use of low p_T muons and recoil calibration of the missing transverse momentum (p_T). However, measurements from high p_T muons require improved lepton calibration, which is the primary focus of this work [17].

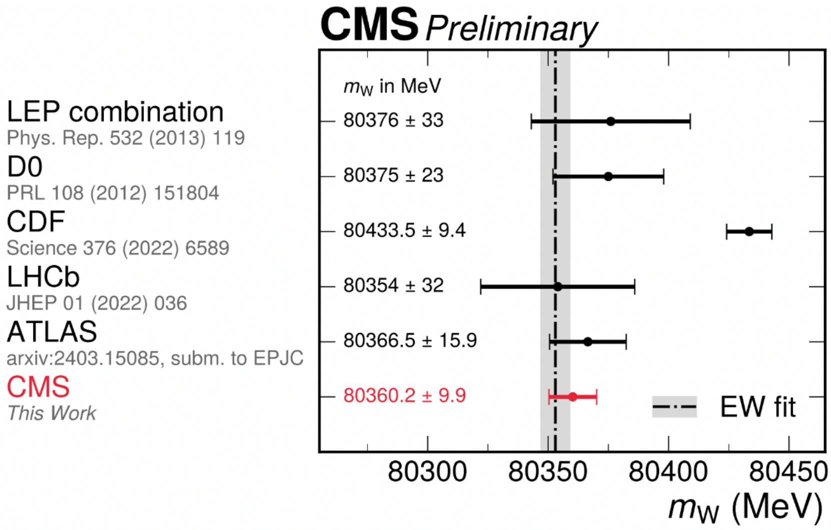

Figure 5.2: Current measurements of the W-Boson mass from major colliders. [18]

5.2.1 Z-boson mass measurement

The mass of the Z boson is measured through different methods in different experiments:

- At the **Tevatron** [19] and **LHC**, the Z boson mass is measured by reconstructing its decay products (Table 5.1). This method relies on the precise measurement of the invariant mass of the lepton pairs or hadrons produced in these decays. The reconstruction of the Z boson mass is achieved by analyzing events from tracking detectors, calorimeters, and muon systems to reconstruct these decays.

Decay Channel	**Branching Ratio (%)**
$Z \to e^+e^-$	3.3632
$Z \to \mu^+\mu^-$	3.3662
$Z \to \tau^+\tau^-$	3.3696
Total Leptonic Decays	10.1
Total Neutrino Decays	20
$Z \to$ hadrons	69.987

Table 5.1: Branching Ratios for Z Boson Decays

- At **LEP** (Large Electron-Positron Collider), the Z boson mass was extracted by analyzing the energy dependence of the cross section for the processes $e^+e^- \to$ hadrons and $e^+e^- \to \ell^+\ell^-$ near the Z resonance. Electron-positron collisions would produce a Z boson near its resonance energy, and the total cross section for these processes exhibits a peak at the Z mass. The mass was extracted by studying the energy distribution and shape of the Z-resonance. The measurement of the width of this peak, alongside the energy dependence, allowed precise determination of both the mass and the total decay width of the Z boson [20].

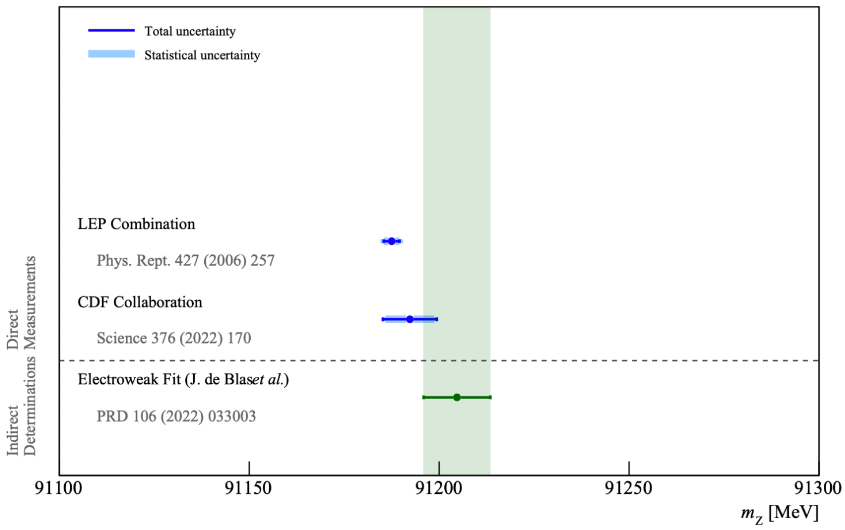

Figure 5.3: Current Status of the Z-Boson mass showing results from LEP and Tevatron.

m_Z measurement at ATLAS

The Z-boson mass at ATLAS is measured by reconstructing lepton decays, with focus on the μ-channel in this study, as it provides clean and distinct signatures. The Z-mass is correlated with the W-mass through the weak mixing angle, highlighting the importance of precise Z-mass measurements at ATLAS. This measurement also serves as a valuable cross-check for validating the methods and calibrations used in the $W^{\pm}$ boson analysis.

Standard muon calibration in ATLAS uses muons from the Z-boson decays as a reference. However, we aim to measure the Z-mass itself after the calibration and muons from the Z-boson would bias our analysis. Hence, muons from the decay of J/ψ mesons were employed for calibration, as J/ψ mesons are produced abundantly at the LHC and their properties are well-known.

5.3 The Large Hadron Collider (LHC) and the ATLAS Detector

The Large Hadron Collider (LHC), located at CERN in Geneva, Switzerland, accelerates protons and heavy ions to nearly the speed of light and collides them at various detectors, including the ATLAS detector [21]. These collisions produce a wide range of particles, including the Z boson, a neutral particle mediating the weak force.

5.3.1 The ATLAS Detector

The ATLAS detector is a large, multi-purpose particle detector at the LHC designed to study particles produced in high-energy collisions. Once particles are accelerated and collide in the LHC, they pass through ATLAS, which consists of several components designed to detect different aspects of particles produced, Fig 5.4:

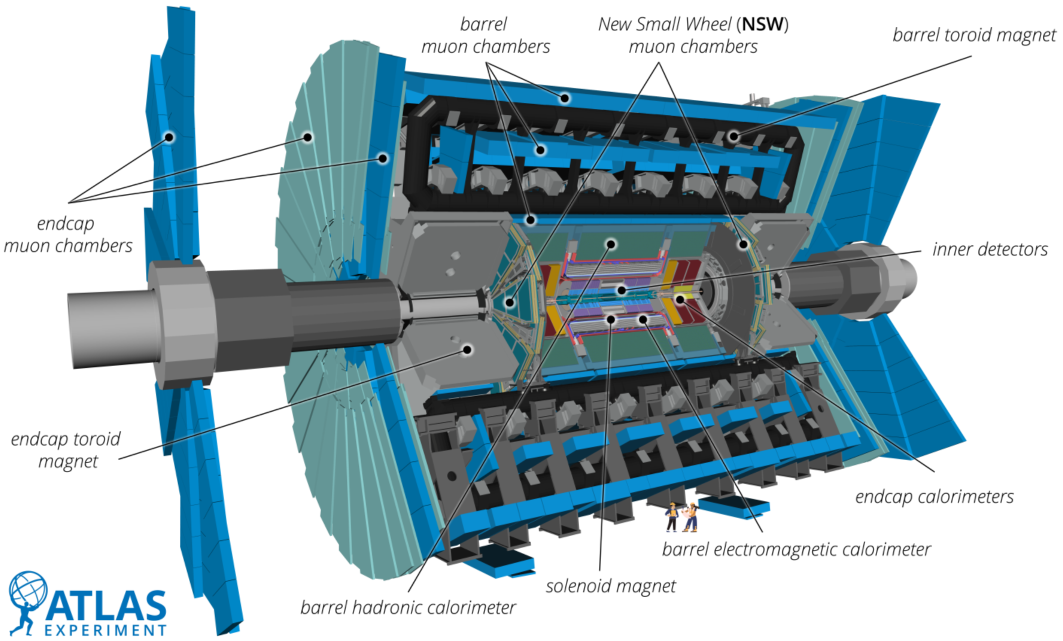

Figure 5.4: Schematic of the ATLAS Detector Layout. [22]

- The **Inner Detector** (ID) is responsible for measuring the trajectories of charged particles. It includes the Pixel Detector, the Semiconductor Tracker (SCT), and the Transition Radiation Tracker (TRT), which help in reconstructing particle interactions and identifying primary vertices.

- The **Solenoid Magnet** surrounds the ID and produces a uniform magnetic field along the axis of the detector. This magnetic field causes charged particles to curve, with the amount of curvature being inversely proportional to their momentum. The solenoid provides information for tracking and momentum determination of particles passing through the ID.

- The Calorimeters are used to measure the energy of particles. The **Electromagnetic Calorimeter** (ECal) measures electron and photon energies, while the **Hadronic Calorimeter** (HCal) measures hadron energies. Both use different materials, such as lead/liquid argon for EM Cal and steel & scintillating tiles for HCal, and measure the energy deposited when these particles interact with the calorimeter material .

- The **Toroid magnets** in ATLAS consist of a large barrel toroid for $|\eta| < 1$ and two smaller toroids for $1.4 < |\eta| < 2.7$ at the endcaps. Each system has eight superconducting coils. The barrel toroid is positioned around the central region, while the endcap toroids are placed beyond the forward calorimeter. These magnets generate a magnetic field in the azimuthal plane, bending particles in the Muon Spectrometer, with the field perpendicular to the particle's flight, deflecting them in the η plane.

- The **Muon Spectrometer** (MS) is designed to identify muons that pass through the calorimeters with little energy loss hence are not detected. The Muon System uses several layers of detectors, including **Drift tubes** (DT), **Resistive Plate Chambers** (RPC), and **tubular wire chambers** to track and measure the muon trajectories. These particles are then distinguished from other charged particles based on their ability to penetrate through the calorimeters without significant energy loss.

While the track reconstruction is performed using the combined tracks from both the Muon System and the Inner Detector, our analysis concentrates on the data provided by the Inner Detector, which will be the focus of 5.3.3.

5.3.2 Co-ordinate System of the ATLAS Detector

ATLAS uses a right-handed co-ordinate system with the z-axis pointing along the beam line and the origin being the primary Interaction Point (IP), which is the location where the protons collide during an event. Cylindrical co-ordinates (r, ϕ) are used for the transverse plane with ϕ being the azimuthal angle around the z-axis and r being the distance from the z-axis. Another quantity, Pseudorapidity (η), is defined as, $\eta = -\ln \tan \theta/2$, where θ is the polar angle in the longitudinal plane. These parameters are illustrated in Fig 5.5.

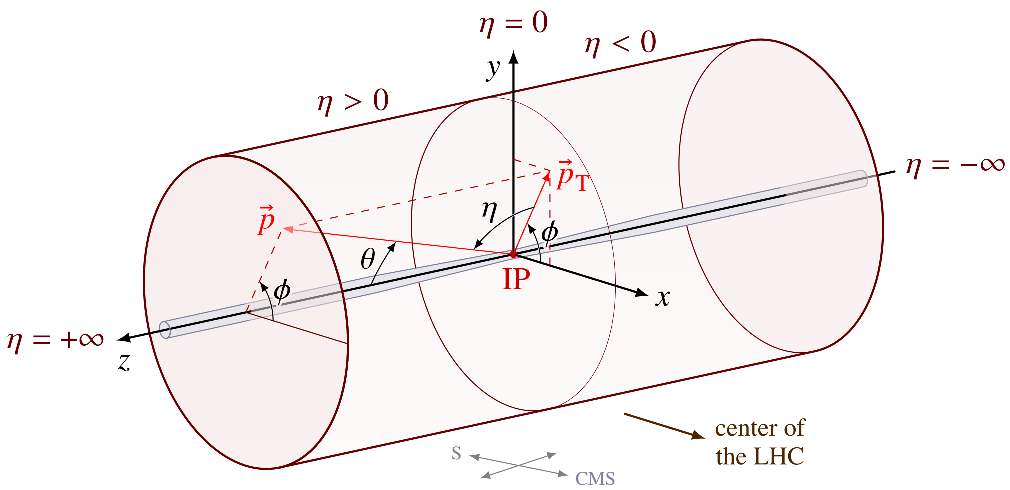

Figure 5.5: ATLAS Co-ordinate system diagram

5.3.3 Inner Detector

The Inner Detector (ID) in ATLAS is the primary tracking system that is located closest to the interaction point and operates within a 2T solenoid magnetic field. The ID consists of three main subdetectors (Fig 5.6): the Pixel Detector, which provides high-resolution tracking near the beamline; the Semiconductor Tracker (SCT), which improves position resolution with multiple layers of silicon strips; and the Transition Radiation Tracker (TRT), which aids in track reconstruction and electron identification. The ID covers a pseudorapidity range of $|\eta| < 2.5$ and is built to offer reliable track reconstruction, high accuracy in measuring momentum and impact parameters, τ-lepton and b-jets tagging and the ability to determine both the primary and secondary vertices of particle tracks.

- **Pixel Detector**: The innermost layers, closest to the beam pipe, providing the highest spatial resolution for vertex reconstruction and momentum measurement. When a charged particle passes through a pixel sensor, it ionizes the silicon material, creating electron-hole pairs. These charges are collected by applying an electric field across the sensor, producing a measurable electrical signal in individual pixels. There are around 92 million pixels in four layers providing a precision of 10 μm.

- **Semiconductor Tracker** (SCT): A system of around 6 million silicon strip detectors that improve track reconstruction and momentum measurement. The layout is optimized such that a particle passes through at least four layers of silicon and measures the track upto a precision of 25 μm. It enhances spatial resolution and helps in distinguishing closely spaced particle tracks.

- **Transition Radiation Tracker** (TRT): The outermost part of the ID, composed of around 300,000 thin gas-filled straw tubes (called ”drift tubes”), each about 4 mm in diameter and up to 1.5 meters long. As charged particles pass through these straws, they ionize the gas inside. The freed electrons drift toward a central wire, producing a signal that marks the particle’s position. It provides additional tracking measurements, pattern recognition and is essential for particle identification.

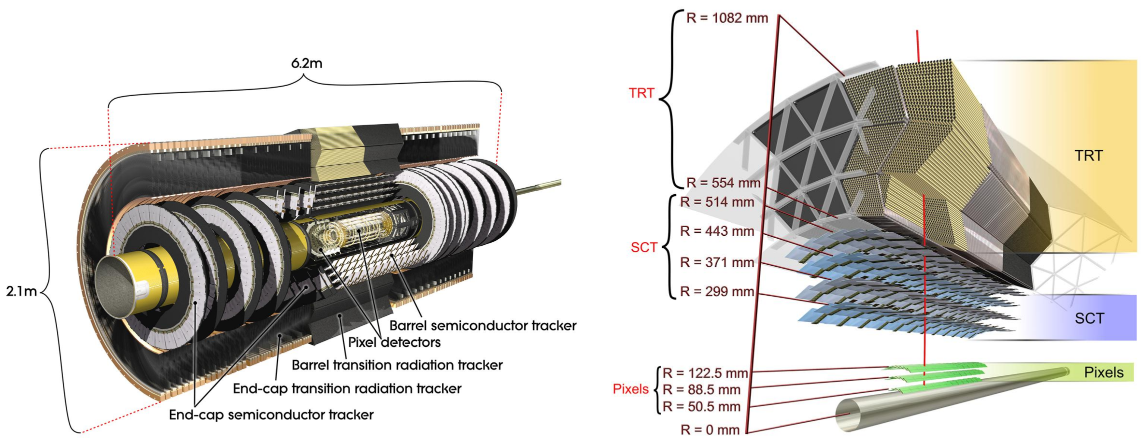

Figure 5.6: Schematics of the Inner Detector system with the components on the right. [23]

Vertex position resolution is crucial for identifying J/ψ mesons originating from b-hadron decays which have a relatively long lifetime (~1.5 ps) and travel a few millimeters before decaying, forming a displaced secondary vertex. This displacement is detected using the impact parameter, which measures the closest approach of decay tracks to the interaction point. In B-hadron decays, J/ψ mesons are produced via weak decays involving interactions with the Z-boson. This process is important for studying the Z-boson mass. The Inner Detector (ID) plays a key role in this measurement, as it provides high-precision tracking data necessary for accurate vertex reconstruction.

5.3.4 Muon Reconstruction

In ATLAS, particle trajectories, known as **tracks**, are reconstructed using hit signals from various detector components. The Inner Detector (ID) and the Muon Spectrometer (MS) serve as the primary systems for track reconstruction. The following parameters (Fig 5.7) are determined by fitting the recorded hit signals to the particle trajectories, which are bent by the magnetic field:

- **Curvature** ($\frac{q}{|p|}$): This denotes the charge of the particle divided by its reconstructed momentum. It is given by
$$\frac{q}{|p|} = \frac{1}{B \times r}$$
where B is the magnetic field strength and r is the radius of the particle's helical trajectory in the magnetic field.

- **Transverse impact parameter** (d_0): The shortest distance between the particle's track and the beam axis in the transverse plane.

- **Longitudinal impact parameter** (z_0): The distance between the particle's track and the interaction point along the beam axis (longitudinal direction).

- **Azimuthal angle** (ϕ): Defines the angle of the particle's trajectory in the transverse plane, same as the definition in 5.3.2.

- **Polar angle** (θ): Represents the angle of the track relative to the beam axis, same as the definition in 5.3.2.

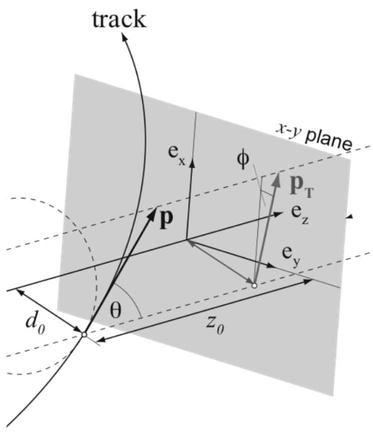

Figure 5.7: Visualization of the track parameters based on the particle trajectory. [24]

Muon reconstruction in ATLAS relies on information from different detector components, including the Inner Detector (ID), the Muon Spectrometer (MS), and the calorimeters. Tracks are first reconstructed independently in the ID and MS, with additional energy deposit data from the calorimeters helping refine the identification. These are then combined for optimal track reconstruction.

There are four types of muon reconstruction based on the detectors involved: **Combined (CB) muons**, which use both ID and MS tracks; **Inner Detector (ID) muons**, identified when an ID track matches a local MS segment; **Calorimeter-tagged (CT) muons**, detected in regions where the MS is inefficient ($\eta < 0.1$) by matching ID tracks to calorimeter energy deposits; and **Extrapolated (ME) muons**, reconstructed solely in the MS for regions where the ID has limited coverage. For more details, please refer to [25].

Please note the in this study, we focus only on the data from muons reconstructed using only the **ID** tracks of muons around the J/ψ resonance at $\sim$ 3.096 GeV.

5.4 Data Acquisition and Trigger Systems

This study utilized Run-2 (2017) data as it has a dedicated B Physics stream which is important for J/ψ production, and has sufficient data for analysis. 2015, 2016, and 2018 data were also explored in [26].

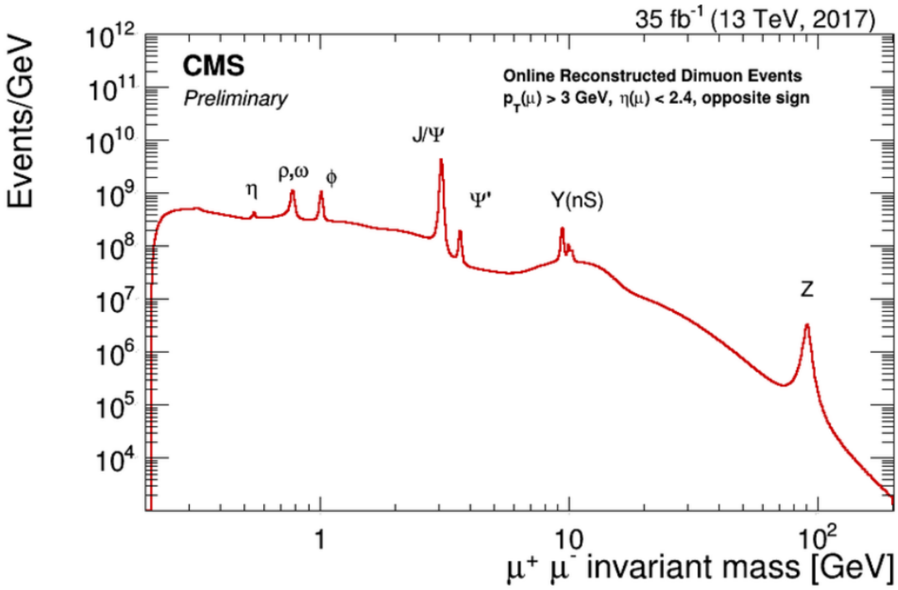

Figure 5.8: Di-muon mass spectrum of CMS from Run-2 data, depicting the amount of J/ψ mesons and Z-bosons. [27]

J/ψ events were used for the calibration of scale and resolution of the muon momentum with the following selections:

1. $2.6 < m_{\mu\mu} < 3.5$ GeV, mass selection around the J/ψ resonance.
2. Quality Working Point: Medium
3. $6.3 < p_{T,leading} < 90$ GeV, not enough statistics for analysis beyond this range.
4. $\mathrm{p}_T^{\mu\mu} > 11$ GeV, simply defined by the trigger selection.
5. Vertex Cut: $|\frac{d_0}{\sigma(d_0)}| < 3$, to minimize the amount of Non-Prompt J/ψ in the samples.
6. Vertex Cut: $|z_0 \sin\theta| < 0.5mm$

5.4.1 Trigger System

In the context of ATLAS, a ”trigger” system is used to select interesting events from the large number of final state particles produced in proton-proton collisions at the LHC. There are about 40 million bunch crossings per second, so the data must be filtered to capture and record the most relevant events. This system combines hardware and software algorithms to decide which events are stored for analysis. It categorizes events into different streams, streamlining the analysis process by grouping data relevant to specific research objectives. The ATLAS Run-2 trigger system consists of two levels: Level 1 (L1) and High-Level Trigger (HLT). L1 makes quick decisions based on calorimeter and muon spectrometer data using hardware components like FPGAs and ASICs, working at a rate of 40 MHz. The HLT, running on CPUs and GPUs, further analyzes the events selected by L1, using data from all ATLAS sub-detectors to categorize them into physics streams, such as b-physics or Higgs physics, based on their signatures.

A significant component of the trigger system is the pre-scale algorithm, which selectively keeps one event every N events, where N is the pre-scale factor. This pre-scale factor is not based on kinematic cuts or any specific selection criteria but rather on a statistical approach to reduce the event rate. For instance, in 2016, b-physics triggers were heavily pre-scaled, making the contributions from the Physics Main and B Physics streams comparable, while in 2017 and 2018, b-physics triggers were not pre-scaled, resulting in a higher contribution from the B Physics stream.

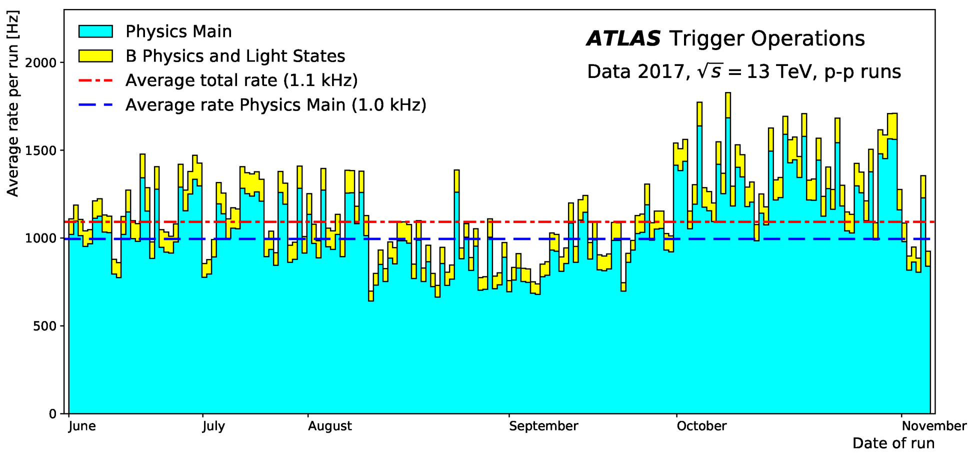

Figure 5.9: Physics Main and B-Physics Trigger rate comparison at ATLAS from 2017 data. [28]

- **Trigger passing** refers to selection of events that satisfy specific kinematic conditions defined by the trigger.

- **Trigger matching** is the process of comparing objects from the triggered event with those reconstructed during the event reconstruction stage (5.3.4). Trigger matching ensures the correct selection of events, since sometimes L1 and HLT trigger system may count events that do not actually satisfy the constraints.

The B Physics stream is rich in J/ψ and Υ mesons, while the Physics Main stream, which focuses on high p_T muons, contains a large number of Z events. Single and double muon triggers from the B Physics and Physics Main streams of the HLT system were used in this study. However, there were some issues with the trigger data that were identified by inspecting individual triggers:

1. Overlap between streams, which was corrected for in the data.

2. Matching flags have bugs and were not applied for this study.

Chapter 6

Muon Momentum Calibration Technique

Accurate muon momentum measurement is important for the ATLAS experiment, as they directly influence the precision of physics analyses. However, various factors, such as detector imperfections (Fig 6.1), reconstruction algorithms, and inaccuracies in the simulation of detector properties, can introduce biases. These biases can distort observables, like invariant mass distributions, and lead to systematic uncertainties that impact the interpretation of results, especially in sensitive analyses such as the Z mass measurement. To mitigate these issues, the ATLAS detector employs an alignment strategy [29, 30], with the Inner Detector (ID) alignment optimized through a global χ^2 minimization of track-to-hit residuals, while the Muon Spectrometer (MS) uses an optical alignment system to ensure proper positioning of the muon chambers. However, biases known as ”weak modes,” involve distortions the alignment cannot detect and still remain in the data which degrades the precision of measurements.

To correct for these biases, ATLAS utilizes a detailed calibration process [31]. After alignment, the Muon Momentum Calibration (MMC) procedure is employed to address charge-dependent effects, geometrical distortions, and mis-modeling of the magnetic field. This procedure accounts for weak modes and Sagitta biases and further addresses the impact of multiple scattering and uncertainties in the magnetic field. By adjusting the reconstructed muon momenta in Monte-Carlo (MC) simulations to match those observed in data, the data-to-simulation agreement is improved. In this study the scale and resolution corrections are calculated and validated.

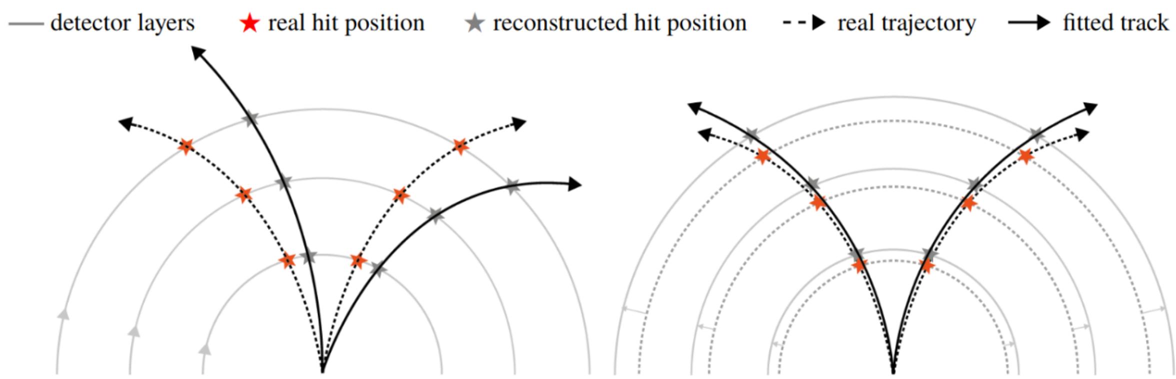

Figure 6.1: Charge Dependent Effects arise from rotations and Sagitta biases (Left), whereas Charge Independent Effects may arise from radial distortions (Right). [32]

6.1 Charge-Dependent Bias

One of the key biases that affect these measurements is the charge-dependent bias, which degrades the momentum resolution. These distortions arise due to detector rotations in the transverse plane and affect Sagitta measurements during tracking. The Sagitta is the distance between the actual curved path of the particle and the straight line (chord) that connects the points where the particle enters and exits a particular detector plane.

These effects are quantified by the Sagitta bias, δ_S, which is expressed by:

$$\frac{q}{\hat{p}} = \frac{q}{p} + \delta s, \tag{5.1}$$

where q is the electric charge, p is the unbiased momentum, $\hat{p}$ is the biased momentum, and δs is the strength of the bias. This bias can be estimated using Eq.6.1 and is obtained by χ^2-minimization of the invariant Di-muon mass with fine binning in η and ϕ.

$$p_T^{corrected} = \frac{p_T^{biased}}{1 + q\delta_s(\eta, \phi)p_T^{biased}} \tag{6.1}$$

Sagitta Correction was already provided and it was implemented on the Ntuples before the calibration procedure was implemented in this study.

6.2 Charge-Independent Bias

Scale and resolution biases in the muon transverse momentum (p_T) can occur due to charge-independent effects, such as mis-modeling of the magnetic field or detector distortions (or weak modes), which are not addressed by the Sagitta correction. This study specifically focuses on calculating these corrections by addressing such charge-independent biases. The corrections are estimated using a dedicated calibration procedure, applying the MCP framework on J/ψ muons in the ID.

6.2.1 Scale and Resolution Corrections

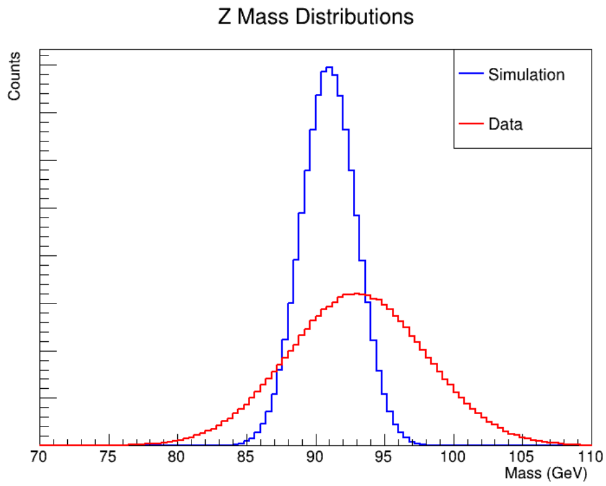

Figure 6.2: Exaggerated sketch for representing how the scale errors shift the mean and resolution biases in the data causes smearing. [26]

Fig 6.2 represents the effects of Scale and resolution biases on a set of hypothetical simulation and data, showing the mass distributions of the Z boson. Data is subject to biases whereas the simulation is the ideal scenario. Scale effects move the mean of the distribution and resolution effects cause smearing. This occurs due to the stochastic as well as distortion effects like:

- **Ionization Loss:** Muons are minimum ionizing particles which lose less energy depending on the medium. In the inner detector, this loss is negligible, but in the calorimeters, it can reach up to 3 GeV, following the Bethe-Bloch formula for energy loss.

- **Multiple Scattering:** Charged particles undergo multiple scattering when interacting with the material's nuclei. This effect is independent of the particle's energy but depends on the material's thickness and radiation length.

- **Magnetic Field:** The magnetic field bends particles, allowing momentum calculation from trajectory curvature. For low-energy particles or a strong magnetic field, the momentum measurement is more accurate, while for high-energy particles or weaker fields, accuracy decreases.

The corrected transverse momentum, $p_T^{Cor,ID}$, is calculated by estimating the Scale and resolution corrections using:

$$p_T^{Cor,ID} = \frac{p_T^{MC,ID} + \sum_{n=0}^{1} \Delta s_n^{ID} (p_T^{MC,ID})^n}{1 + \sum_{m=0}^{2} \Delta r_m^{ID} (p_T^{MC,ID})^{m-1} g_m} \tag{6.2}$$

$\mathbf{\Delta s_n^{ID}}$: Scale corrections

- $\mathbf{\Delta s_0^{ID}}$: Constant scale correction accounting for low muon p_T energy loss, which is significant only for MS and CB tracks. Since we only consider the ID track, there is no material budget before the ID where the muon looses energy hence this quantity set to zero.

- $\mathbf{\Delta s_1^{ID}}$: Corrects for inaccuracy in the description of the magnetic field integral and the radial distortions.

$\mathbf{\Delta r_m^{ID}}$: Resolution smearing corrections

- $\mathbf{\Delta r_0^{ID}}$: Accounts for fluctuations of the energy loss in the traversed material. Again since there is negligible energy loss in the ID, we set this quantity to zero.

- $\mathbf{\Delta r_1^{ID}}$: Accounts for multiple scattering, uncertainties and inhomogeneities in the modeling of the local magnetic field, and radial distortions of the detector layers.

- $\mathbf{\Delta r_2^{ID}}$: Describes intrinsic resolution effects of the detector and residual mis-alignments between the different detector elements.

6.3 Calibration Methodology

The correction parameters from Eq.6.2 are extracted from data using an iterative fitting procedure that compares the invariant mass distributions for $J/\psi \rightarrow \mu\mu$ and $Z \rightarrow \mu\mu$ evnets in data and simulation.

The calibration fit was initially performed by using η as the variable for the correction parameters, followed by ϕ, and finally p_T. The binning defined for each case were:

- 12 regions were made for the η-calibration, avoiding the end-cap regions of the ID with the selection: $|\eta| < 1.05$.
- 16 regions were made for the ϕ-calibration.
- 10 regions were made for the p_T-calibration. (Resolution parameters ignored in this case since p_T-calibration is assumed to be independent of resolution effects)

The calibration framework follows a step-by-step algorithm in each iteration, as outlined below:

1. **Corrections:** At the beginning of each iteration, two types of corrections are applied to the muon p_T for both data and Monte Carlo (MC) samples. For data, the p_T is corrected using the Sagitta bias correction. For MC, the p_T is corrected based on scale and resolution parameters derived from the previous iteration.

2. **Muon Selection:** In the initial iterations of the calibration process, only muons from the same region are selected for fitting, according to the binning scheme defined earlier. This is important because each region may require different correction parameters. If muons from different regions were fit together, they would receive the same correction, which may be incorrect.

   In later iterations, however, the correction parameters are determined by fitting muons from different regions together. The values of the correction parameters for each region are initialized using the results from the previous iteration. This approach allows for more refined corrections, as it gradually adjusts the parameters for each region based on the latest fits.

3. **Background estimation:** After filling the histograms, the J/ψ background is estimated using an parametric exponential or Chebyshev background of the second order, and by fitting them to the data distribution, an estimate of the background shape and yield is obtained. The signal is estimated by a Crystal ball + Gaussian function:

$$N_{signal} = N \times (\text{Gauss}(\mu_1, \sigma_1) + \text{CB}(\mu_2, \sigma_2, \alpha, \eta)) \tag{6.3}$$

where N is a normalization factor between the Crystal Ball and Gaussian functions. The Crystal Ball function combines a Gaussian core for the central peak region and a power-law tail for deviations, making it ideal for asymmetric distributions. The Crystal Ball function is defined as:

$$f(x; \alpha, n, \mu, \sigma) = \begin{cases} \exp\left(-\frac{(x-\mu)^2}{2\sigma^2}\right), & \text{for } \frac{x-\mu}{\sigma} > -\alpha \\ AB\left(\frac{x-\mu}{\sigma}\right)^{-n}, & \text{for } \frac{x-\mu}{\sigma} \leq -\alpha \end{cases} \tag{6.4}$$

Where the normalization factor A and the continuity parameter B are given by:

$$A = \left(\frac{n}{|\alpha|}\right)^n \exp\left(-\frac{|\alpha|^2}{2}\right)$$

and

$$B = \frac{n}{|\alpha|} - |\alpha|$$

Parameters:

- x: the variable of interest (e.g., energy or mass),
- μ: the peak position or mean of the Gaussian core,
- σ: the standard deviation of the Gaussian core,
- α: the parameter that defines the point where the Gaussian core transitions into the power-law tail (on the left-hand side of the peak),
- n: the exponent that controls the shape of the power-law tail.

4. **Minimization Procedure:** A basic χ^2 minimization algorithm is first used to obtain initial estimates for the parameters which are then used in a likelihood minimization algorithm (Minuit algorithm [33]), which applies the signal and simulation templates with varying

correction parameters and interpolates between them. The procedure involves two types of minimizer:

- Simplex Minimizer: This minimizer first calculates scale parameters by comparing the mean of data and MC distributions using a χ^2 test. It then determines resolution parameters by comparing both the mean and standard deviation. Finally, a binned χ^2 is applied to adjust all parameters simultaneously.
- GridScan Minimizer: Here the corrections are refined by creating a grid of templates around the Simplex minimization results. It calculates the negative log-likelihood for each grid point and interpolates between the values, producing a continuous likelihood function in the calibration parameter space.

6.3.1 Validation Framework

A validation framework to compare calibration across multiple parameters was developed in [26] and applied to validate the results of this study. This framework is designed to identify non-closures, asymmetries, or mis-modelings in the detector regions that require further attention. It applies the correction parameters obtained after the calibration to the MC samples, re-weights them to match the data, and corrects for the Sagitta bias.

Chapter 7

Results and Discussion

7.1 η-Calibration Results

The values of the correction parameters obtained for each η region can be found in Fig 7.1.

After the validation (Fig 7.2), we can clearly observe that the the difference between the data and MC have become flat in the η-spectrum. Whereas, variations in ϕ and p_T can still be seen, which motivates us to proceed with the other calibrations.

7.1.1 $\Delta\phi$ - Study

During the course of this thesis, another effect on the correction parameters was studied based on *Cowboy* and *Sailor* events (Fig 7.3). In the case of a *Cowboy* event, the two daughter tracks might cross in a way that they could share hits, and end up with lower quality reconstructed muons which could be rejected by the trigger or the analysis. While a *Sailor* event is not subject to these issues since the daughter tracks are less likely to be misinterpreted. It doesn't require as many special cuts, unlike the cowboy decay topology [34].

In order to separate these two kinds of events, two selections were made on, $\Delta\phi = \phi_{\mu_+} - \phi_{\mu_-}$, defined as the difference of ϕ between the two decay muons. $\Delta\phi > 0$ selection was made for Sailor events while $\Delta\phi < 0$ selection was made for Cowboy events. After calibrating with these selections (Fig 7.5), a small but consistent effect was seen on the scale parameter which implies that Cowboy or Sailor topologies may affect the p_T distribution of the muons.

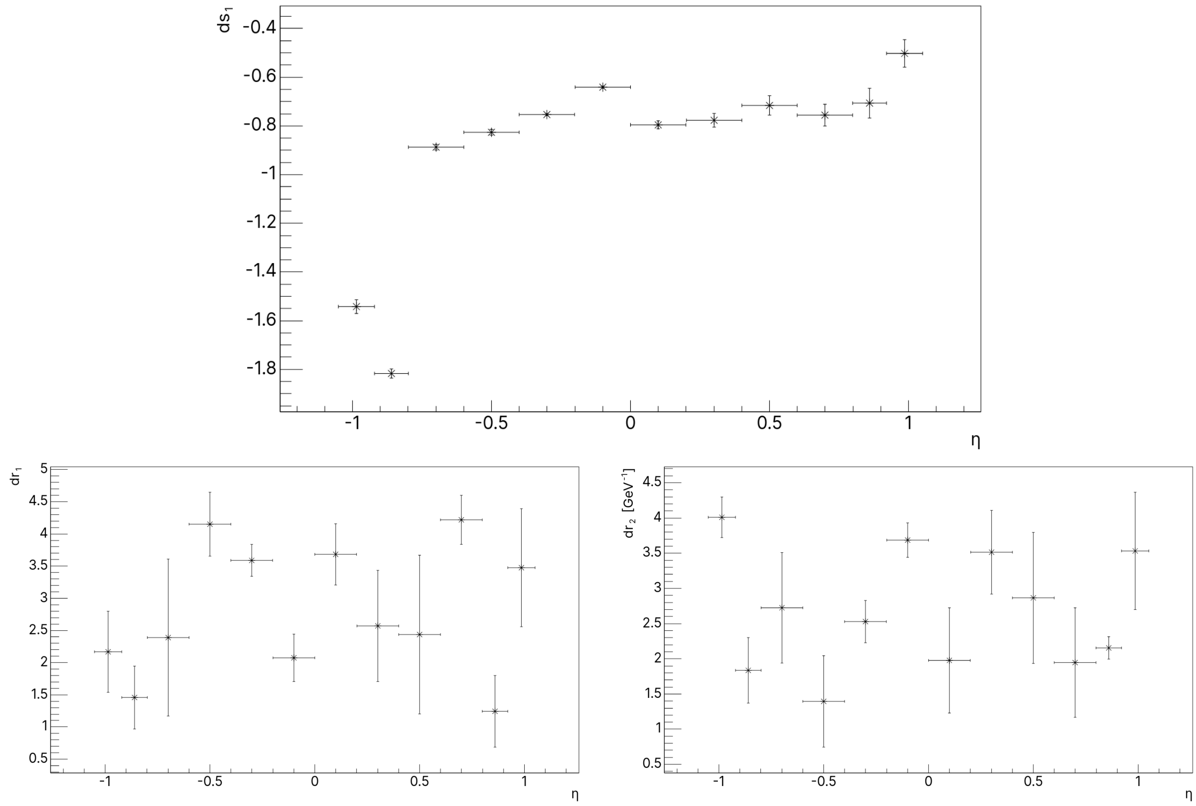

Figure 7.1: η-dependence of muon momentum calibration parameters from 2017 ATLAS data. Top: Scale correction (Δs_1^{ID}) versus η. Bottom: Resolution parameters Δr_1^{ID} (left) and Δr_2^{ID} (right) showing the η-dependent smearing corrections.

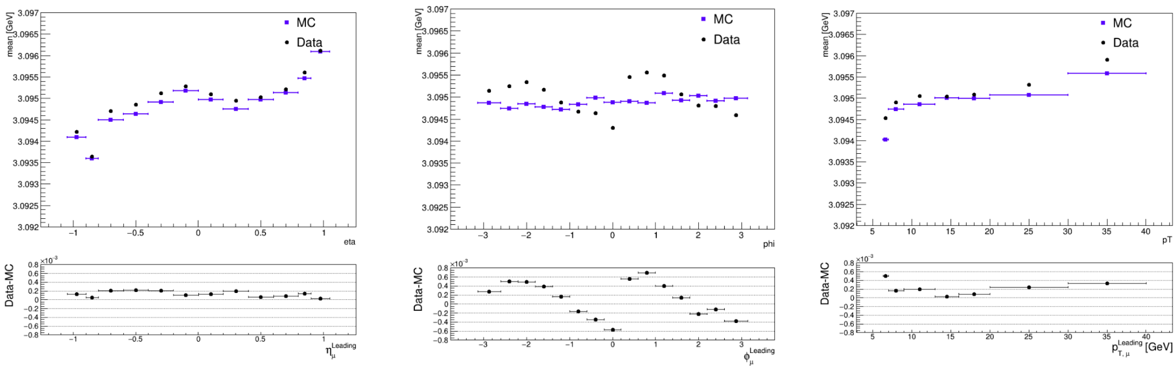

Figure 7.2: η-validation results. The corrected simulation momenta is within 0.05% Data. The flat residual confirms proper η-dependence calibration

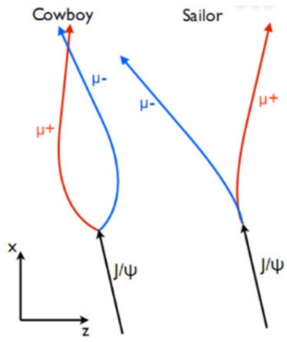

Figure 7.3: Schematic of the Cowboy and Sailor decay topologies at LHC.

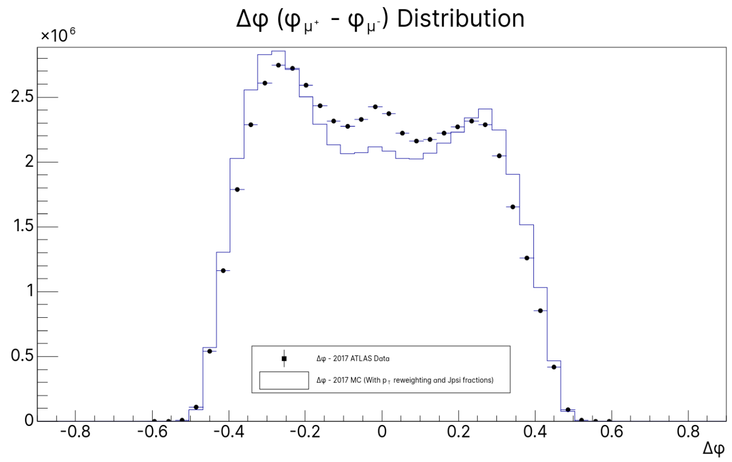

Figure 7.4: Histogram representing the asymmetry in $\Delta\phi$ caused by different trigger rates of Cowboy and Sailor events. Cowboy events have a smaller trigger rates and hence give a smaller peak in the histogram.

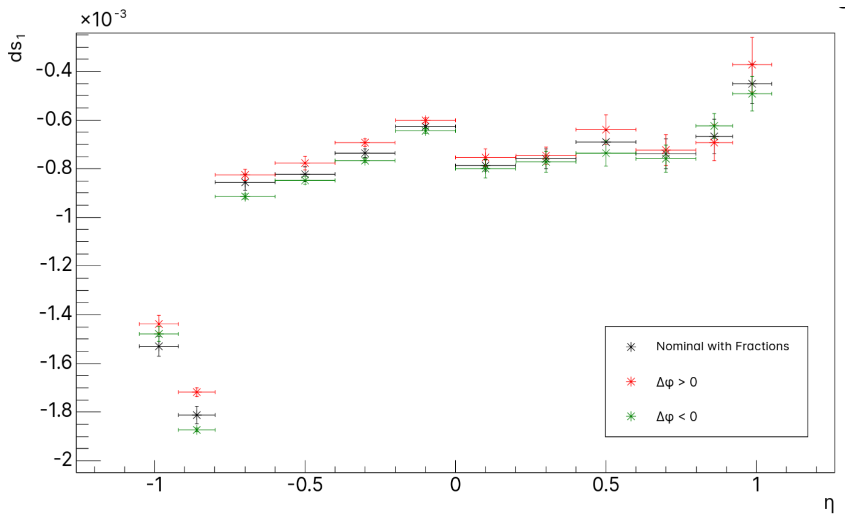

Figure 7.5: η-Calibration result after $\Delta\phi$ selections to see the effects of different trigger rates on the scale parameter.

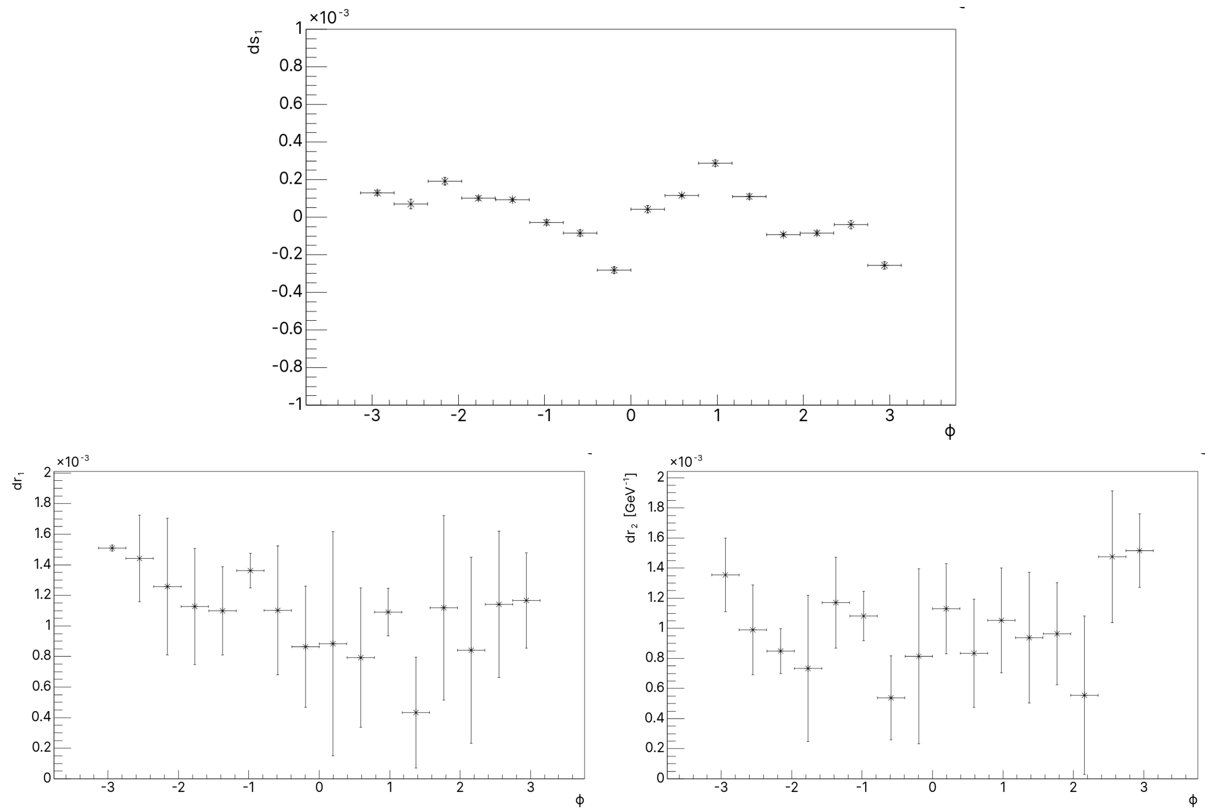

Figure 7.6: ϕ-dependence of muon momentum calibration parameters from 2017 ATLAS data. Top: Scale correction (Δs_1^{ID}) versus ϕ azimuthal angle. Bottom: Resolution parameters Δr_1^{ID} (left) and Δr_2^{ID} (right) showing the ϕ-dependent smearing corrections.

7.2 ϕ-Calibration Results

The values of the correction parameters obtained for each ϕ region can be found in Fig 7.6.

Post validation (Fig 7.7), one can clearly see that the corrections to the ϕ-spectrum has improved the agreement between data and MC, although some asymmetry around zero is still observed. This is probably due to mis-modeling of the magnetic field and has to be accounted for in future calibrations. Furthermore, no significant changes in the η and p_T-spectrum have been observed which further solidifies that each of these calibrations are independent of one another.

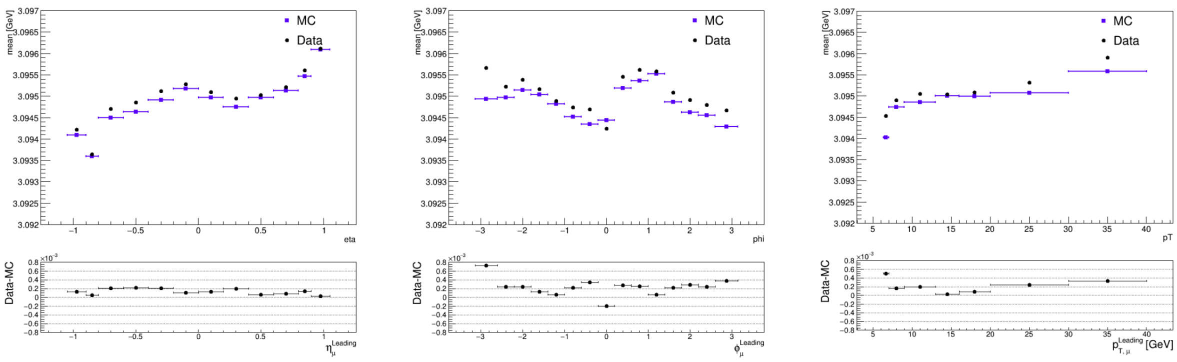

Figure 7.7: ϕ-Validation results. Residual ϕ-dependent biases are reduced to $< 0.1\%$ after calibration.

7.3 p_T-Calibration Results

7.3.1 Prompt and Non-Prompt J/ψ:

Apart from the standard calibration procedure, a different calibration procedure was also applied with weights to filter Non-prompt J/ψ from the data. Prompt and non-prompt J/ψ mesons have different production mechanisms, which lead to different impacts on the p_T distributions. A different p_T distribution would lead to different values of the scale parameter after the calibration.

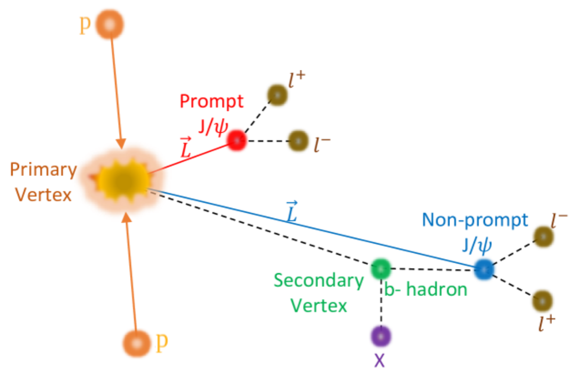

Figure 7.8: Representation of Prompt and Non-Prompt J/ψ decays at LHC.

Prompt J/ψ mesons are produced directly in the primary collision and typically have little to no displacement from the primary vertex, contributing to a p_T distribution that reflects the characteristics of the initial hard scatterings.

On the other hand, **Non-prompt J/ψ mesons**, which originate from the decay of longer-lived particles such as B-hadrons, exhibit a measurable displacement from the primary vertex

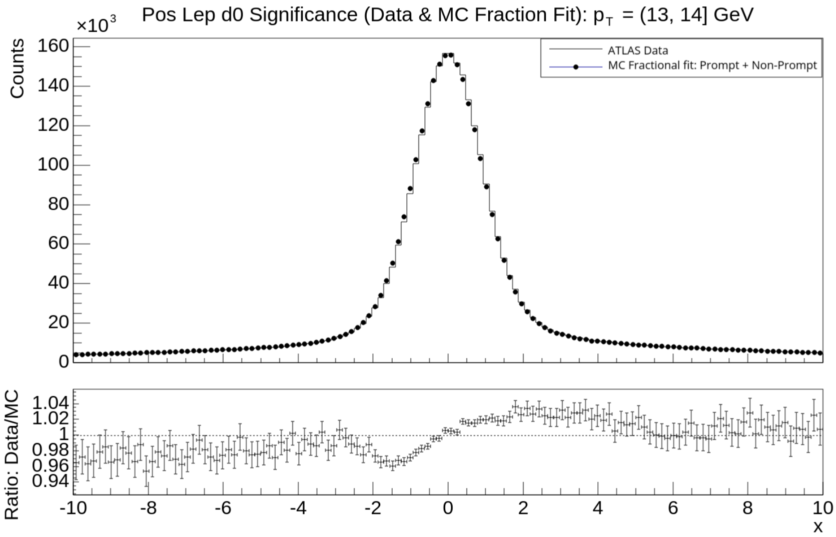

Figure 7.9: Fractional fit result in one of the p_T bins with x-axis as d_0 significance.

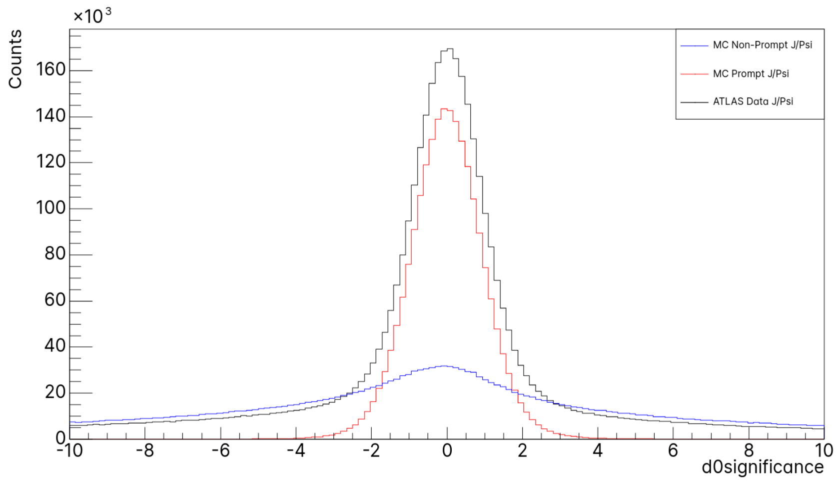

Figure 7.10: Decomposition of the Prompt and Non-prompt MC after applying the fractions.

(non-zero transverse impact parameter, d_0) due to the B-hadrons extended lifetime. This often leads to different kinematic distributions. Thus, estimating the fractions of these two types of J/ψ mesons was a part of this study. Furthermore, Non-prompt J/ψ contained more background in the data and it was advantageous to filter the same.

These fractions were estimated using the TFractionFitter class in ROOT on ten different p_T bins of the MC sample. Refer to Fig 7.9 and 7.10 for the results. The fractions obtained are consistent with previous results from CMS (Fig 7.11) and were then input in the calibration as weights to the prompt MC samples.

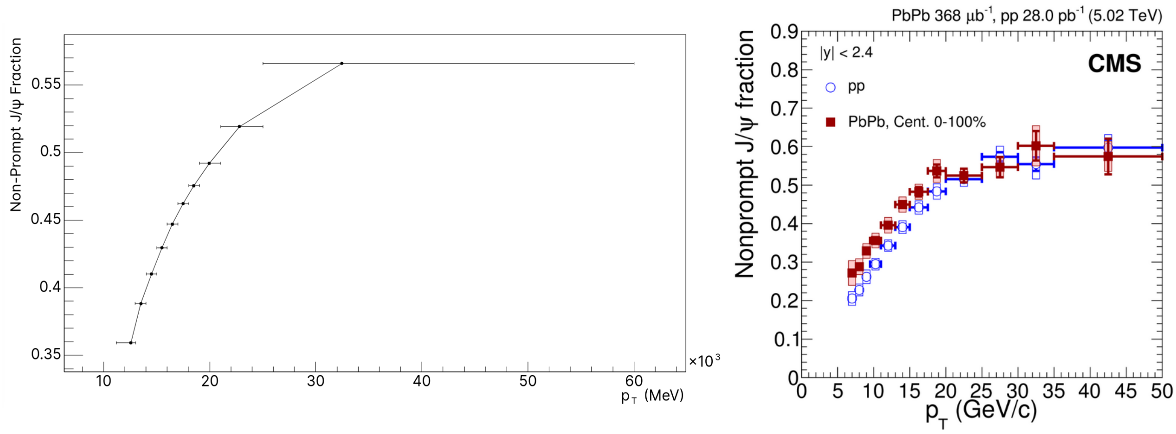

Figure 7.11: Non-prompt fractions obtained after fitting (Left) as compared to the results from CMS (Right) [35]

7.3.2 Scale Calibration Result

Finally, after the calibration the scale correction parameter was obtained (Fig 7.12) and when compared with results obtained by ATLAS, [17] as well as [26], the scale parameter values were consistent. A small resolution effect is also observed for high p_T muons (Fig 7.13) and it

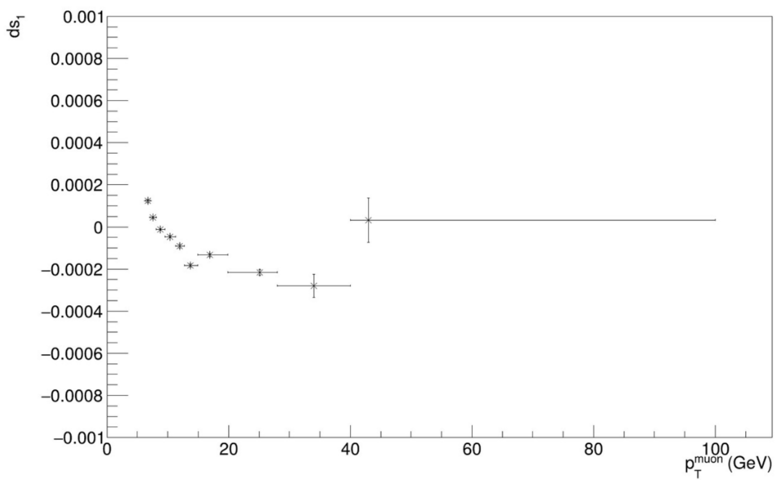

Figure 7.12: p_T-Calibration result for the scale parameter. The jump at high p_T suggests the need for finer resolution in scale parameter to capture the momentum dependence.

may be due to very small number of events. This was considered and the resolution parameter, Δr_2 was introduced to the p_T-Calibration but conclusive results are yet to be analyzed.

Although the correction obtained after applying the fraction is promising (Fig 7.14), the results are not consistent with results obtained by using data from other years. The application and estimation of fractions hence needs to be examined more.

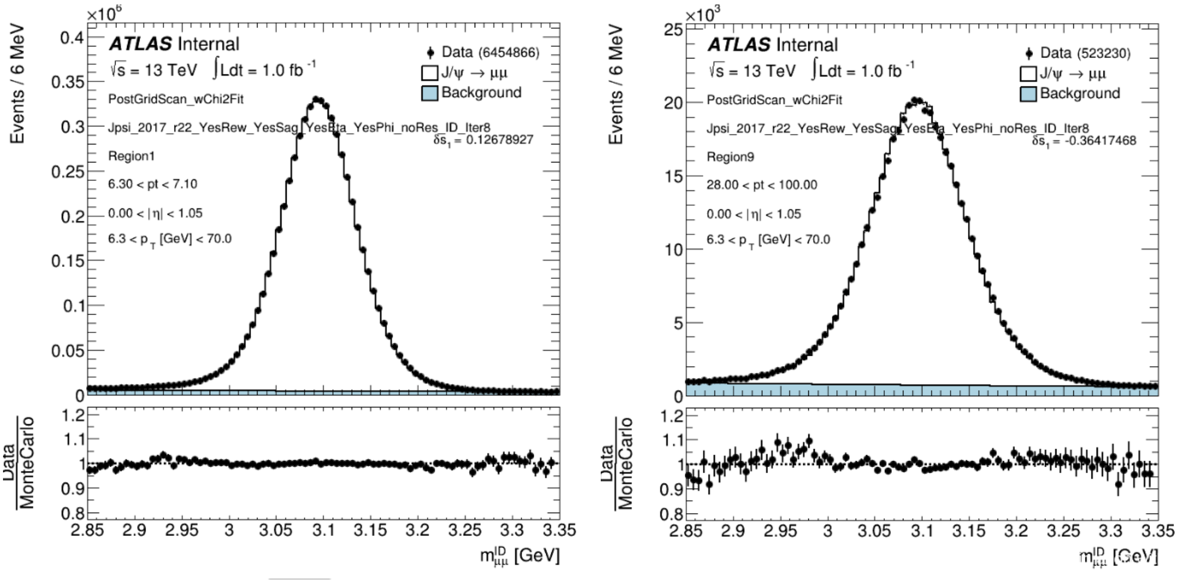

Figure 7.13: Invariant Mass Distribution of Low (Left) and High (right) p_T muons after the calibration showing the resolution effects.

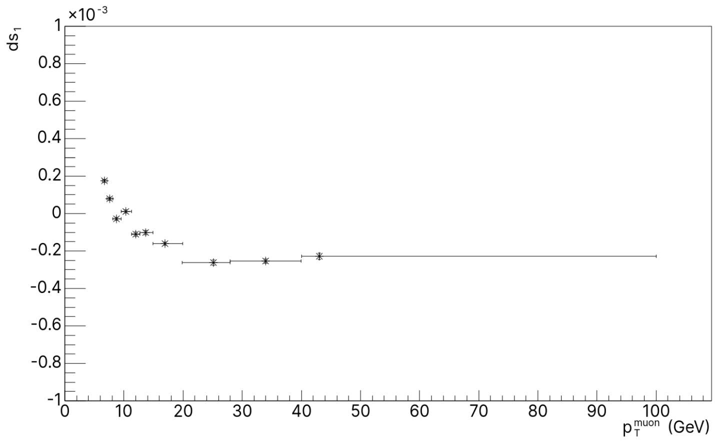

Figure 7.14: p_T-Calibration result for the scale parameter with the Prompt and Non-prompt J/ψ fractions applied.

These are good results since it implies extrapolation of these corrections to the Z-resonance is possible for the calibration of the Z-mass measurement but more statistics and analysis in regions of high p_T is advised.

Chapter 8

Conclusion

This thesis has presented a study of particle detection and measurement across two parts, trying to elucidate why precision is not merely a technical goal, but a way for deeper fundamental understanding. First, the measurement of the ^{12}C+^{12}C fusion cross-section at $E_{cm} = 5.02$ MeV and the confirmation of the $J^{\pi} = 2^{+}$ resonance in ^{24}Mg provides experimental constraints for stellar nucleosynthesis models. These results directly impact our ability to predict carbon burning rates in massive stars and the abundance of elements in stars. Future work may include analyzing data from the S1 and PIXEL detector, which covers intermediate angles. Additionally, exploring other important channels, such as the α_3-channel, (which puts a hard constraint on the spin assignment), may serve as a validation for the results obtained in this study.

Second, the muon momentum calibration studies demonstrate consistent scale corrections across multiple years when compared with reference analyses, though more statistics is needed to validate the extrapolation to high-p_T regions. While p_T-calibration was initially treated as resolution-independent, small but observable effects emerge for high-p_T muons, suggesting future analyses should incorporate resolution parameters. The $\Delta\phi$ asymmetry between Cowboy and Sailor topologies affects the η-calibration, implying that trigger rate differences must be accounted for. Additionally, the inclusion of prompt/non-prompt J/ψ fractions impacts the scale calibration, although inconsistencies indicate either unaccounted effects or new models are needed. Furthermore, [17] identifies more ID distortions in the form of weak modes that are not corrected by this calibration procedure and may have an effect on the Z-Mass measurements.

The continued refinement of these measurement techniques may contribute to yield further insights into both stellar processes and the fundamental interactions described by the Standard Model.

Bibliography

[1] Jean Nippert. “Quantum tunneling fusion reactions with impact on massive stars with STELLA”. 2023STRAE015. PhD thesis. École doctorale Physique et chimie-physique (Strasbourg), 2023. URL: http://www.theses.fr/2023STRAE015/document.

[2] *EXFOR - Experimental Nuclear Reaction Data.* URL: https://www-nds.iaea.org/exfor/.

[3] C. de Loore and C. Doom. *Structure and Evolution of Single and Binary Stars*. Astrophysics and Space Science Library. Springer Netherlands, 1992. ISBN: 9780792317685. URL: https://books.google.fr/books?id=LJgNIi0vkeYC.

[4] Daniel Santiago-Gonzalez et al. “Fusion measurements of 12 C+ 12 C at energies of astrophysical interest”. In: *EPJ Web of Conferences* 117 (May 2016), p. 09011. DOI: 10.1051/epjconf/201611709011.

[5] Erich W. Vogt. “R-matrix Theory*”. In: 2005. URL: https://api.semanticscholar.org/CorpusID:18280611.

[6] W. Galster et al. “Spin assignments for the sub-Coulomb resonances of the ^{12}C + ^{12}C reaction”. In: *Phys. Rev. C* 15 (3 Mar. 1977), pp. 950–953. DOI: 10.1103/PhysRevC.15.950. URL: https://link.aps.org/doi/10.1103/PhysRevC.15.950.

[7] John M. Blatt and L. C. Biedenharn. “The Angular Distribution of Scattering and Reaction Cross Sections”. In: *Rev. Mod. Phys.* 24 (4 Oct. 1952), pp. 258–272. DOI: 10.1103/RevModPhys.24.258. URL: https://link.aps.org/doi/10.1103/RevModPhys.24.258.

[8] H. W. Becker et al. "The12C+12C reaction at subcoulomb energies (II)". In: *Zeitschrift für Physik A Atoms and Nuclei* 303.4 (Dec. 1981), pp. 305–312. DOI: 10.1007/BF01421528. URL: https://doi.org/10.1007/BF01421528.

[9] Michael G. Mazarakis and William E. Stephens. "Experimental Measurements of the ^{12}C + ^{12}C Nuclear Reactions at Low Energies". In: *Phys. Rev. C* 7 (4 Apr. 1973), pp. 1280–1287. DOI: 10.1103/PhysRevC.7.1280. URL: https://link.aps.org/doi/10.1103/PhysRevC.7.1280.

[10] E. F. Aguilera et al. "New γ-ray measurements for ^{12}C+^{12}C sub-Coulomb fusion: Toward data unification". In: *Phys. Rev. C* 73 (6 June 2006), p. 064601. DOI: 10.1103/PhysRevC.73.064601. URL: https://link.aps.org/doi/10.1103/PhysRevC.73.064601.

[11] E. Almqvist et al. "Spins and Partial Widths of Quasimolecular Resonances in C^{12}+C^{12} Interactions". In: *Phys. Rev.* 130 (3 May 1963), pp. 1140–1152. DOI: 10.1103/PhysRev.130.1140. URL: https://link.aps.org/doi/10.1103/PhysRev.130.1140.

[12] C. L. Jiang et al. "Heavy-ion fusion reactions at extreme sub-barrier energies". In: *The European Physical Journal A* 57.7 (July 2021). ISSN: 1434-601X. DOI: 10.1140/epja/s10050-021-00536-2. URL: http://dx.doi.org/10.1140/epja/s10050-021-00536-2.

[13] M. Pignatari et al. "THE12C +12C REACTION AND THE IMPACT ON NUCLEOSYNTHESIS IN MASSIVE STARS". In: *The Astrophysical Journal* 762.1 (Dec. 2012), p. 31. ISSN: 1538-4357. DOI: 10.1088/0004-637x/762/1/31. URL: http://dx.doi.org/10.1088/0004-637X/762/1/31.

[14] P. Eggenberger et al. "The Geneva stellar evolution code". In: *Astrophysics and Space Science* 316.1–4 (June 2007), pp. 43–54. ISSN: 1572-946X. DOI: 10.1007/s10509-007-9511-y. URL: http://dx.doi.org/10.1007/s10509-007-9511-y.

[15] A V Bednyakov. "Quantum field theory and the electroweak Standard Model". In: (2022). DOI: 10.23730/CYRSP-2021-005.1. URL: https://cds.cern.ch/record/2841931.

[16] R Ofierzynski. "W boson mass and properties at LEP". In: *Journal of Physics: Conference Series* 110.4 (May 2008), p. 042019. ISSN: 1742-6596. DOI: 10.1088/1742-6596/110/4/042019. URL: http://dx.doi.org/10.1088/1742-6596/110/4/042019.

[17] Andres Pinto Pinoargote. "Measurement of the W-Boson Mass with the ATLAS Detector at the LHC". English. PhD thesis. Université Paris-Saclay; Johannes Gutenberg-Universität Mainz, 2024.

[18] CMS Collaboration. *Measurement of the W boson mass in proton-proton collisions at $\sqrt{s} = 13$ TeV*. Tech. rep. Geneva: CERN, 2024. URL: https://cds.cern.ch/record/2910372.

[19] CDF Collaboration. "High-precision measurement of the W boson mass with the CDF II detector". In: *Science* 376.6589 (2022), pp. 170–176. DOI: 10.1126/science.abk1781.

[20] "Measurement of the mass of the Z boson and the energy calibration of LEP". In: *Physics Letters B* 307.1 (1993), pp. 187–193. ISSN: 0370-2693. DOI: https://doi.org/10.1016/0370-2693(93)90210-9. URL: https://www.sciencedirect.com/science/article/pii/0370269393902109.

[21] Stephen Myers. "THE LARGE HADRON COLLIDER 2008–2013". In: *International Journal of Modern Physics A* 28.25 (2013). DOI: 10.1142/S0217751X13300354.

[22] Riccardo Maria Bianchi and ATLAS Collaboration. "ATLAS experiment schematic or layout illustration". General Photo. 2022. URL: http://cds.cern.ch/record/2837191.

[23] Joao Pequenao. "Computer generated image of the ATLAS inner detector". General Photo. 2008. URL: https://cds.cern.ch/record/1095926.

[24] Peter Hansen. *Track Reconstruction*. NordForsk lectures. URL: https://indico.nbi.ku.dk/event/454/contributions/2087/attachments/620/944/trackalgs-temp.pdf.

[25] D. Vannicola. "Muon Reconstruction and Identification in the ATLAS Experiment at LHC". In: *Frascati Phys. Ser.* 67 (2018). Ed. by Gennaro Corcella, pp. 94–98. URL: https://cds.cern.ch/record/2677374.

[26] Dionysios Fakoudis. "Precise muon momentum calibration and Z mass measurement with the ATLAS experiment, using pp collisions at $\sqrt{s} = 13$ TeV". English. High Energy Physics - Experiment [hep-ex]. PhD thesis. Université Paris-Saclay; Johannes Gutenberg-Universität Mainz, 2024. URL: https://tel.archives-ouvertes.fr/tel-04957493.

[27] Swagata Mukherjee. “Data Scouting and Data Parking with the CMS High level Trigger”. In: *PoS* EPS-HEP2019 (2020), p. 139. DOI: 10.22323/1.364.0139. URL: http://cds.cern.ch/record/2766071.

[28] *Trigger Menu in 2017*. Tech. rep. All figures including auxiliary figures are available at https://atlas.web.cern.ch/Atlas/GROUPS/PHYSICS/PUBNOTES/ATL-DAQ-PUB-2018-002. Geneva: CERN, 2018. URL: https://cds.cern.ch/record/2625986.

[29] ATLAS Collaboration. “Alignment of the ATLAS Inner Detector in Run 2”. In: *The European Physical Journal C* 80.12 (Dec. 2020). ISSN: 1434-6052. DOI: 10.1140/epjc/s10052-020-08700-6. URL: http://dx.doi.org/10.1140/epjc/s10052-020-08700-6.

[30] *Performance of the muon spectrometer alignment in 2017 and 2018 data*. Tech. rep. Geneva: CERN, 2021. URL: https://cds.cern.ch/record/2753329.

[31] The ATLAS Collaboration. “Studies of the muon momentum calibration and performance of the ATLAS detector with pp collisions at $\sqrt{s} = 13$ TeV”. In: *The European Physical Journal C* 83.8 (Aug. 2023). ISSN: 1434-6052. DOI: 10.1140/epjc/s10052-023-11584-x. URL: http://dx.doi.org/10.1140/epjc/s10052-023-11584-x.

[32] ATLAS Collaboration. “Experiment Briefing: Keeping the ATLAS Inner Detector in perfect alignment”. General Photo. 2020. URL: https://cds.cern.ch/record/2723878.

[33] F. James and M. Roos. “Minuit - a system for function minimization and analysis of the parameter errors and correlations”. In: *Computer Physics Communications* 10.6 (Dec. 1975), pp. 343–367. ISSN: 0010-4655. DOI: 10.1016/0010-4655(75)90039-9. URL: http://dx.doi.org/10.1016/0010-4655(75)90039-9.

[34] T. Schuster. *Production of Neutral Strange Hadrons with High Transverse Momentum in Pb+Pb Collisions at 158 A GeV*. 2006. URL: https://books.google.fr/books?id=QcJ20AEACAAJ.

[35] CMS Collaboration. “Measurement of prompt and nonprompt charmonium suppression in PbPb collisions at 5.02 TeV”. In: *The European Physical Journal C* 78.6 (June 2018). ISSN: 1434-6052. DOI: 10.1140/epjc/s10052-018-5950-6. URL: http://dx.doi.org/10.1140/epjc/s10052-018-5950-6.